Syntaxin 17 recruitment to mature autophagosomes is temporally regulated by PI4P accumulation

Authors: Saori Shinoda[1,4], Yuji Sakai[1,2], Takahide Matsui[3], Masaaki Uematsu[1,5], Ikuko Koyama-Honda[1], Jun-ichi Sakamaki[1,6], Hayashi Yamamoto[1,3], Noboru Mizushima[1,*]

Affiliations:

[1] Department of Biochemistry and Molecular Biology, Graduated School of Medicine, The University of Tokyo, Tokyo, Japan

[2] Department of Biosystems Science, Institute for Life and Medical Sciences, Kyoto University, Kyoto, Japan

[3] Department of Molecular Oncology, Institute for Advanced Medical Sciences, Nippon Medical School, Tokyo, Japan

[4] Present address: Faculty of Life Sciences, Kyoto Sangyo University, Kyoto, Japan

[5] Present address: Weill Institute for Cell and Molecular Biology, Cornell University, New York, USA

[6] Present address: Department of Physiology, Juntendo University Graduate School of Medicine, Tokyo, Japan

* Correspondence to: N. Mizushima (e-mail: nmizu@m.u-tokyo.ac.jp)

Abstract:

During macroautophagy, cytoplasmic constituents are engulfed by autophagosomes. Lysosomes fuse with closed autophagosomes but not with unclosed intermediate structures. This is achieved in part by the late recruitment of the autophagosomal SNARE syntaxin 17 (STX17) to mature autophagosomes. However, how STX17 recognizes autophagosome maturation is not known. Here, we show that this temporally regulated recruitment of STX17 depends on the positively charged C-terminal region of STX17. Consistent with this finding, mature autophagosomes are more negatively charged compared with unclosed intermediate structures. This electrostatic maturation of autophagosomes is likely driven by the accumulation of phosphatidylinositol 4-phosphate (PI4P) in the autophagosomal membrane. Accordingly, dephosphorylation of autophagosomal PI4P prevents the association of STX17 to autophagosomes. Furthermore, molecular dynamics simulations support PI4P-dependent membrane insertion of the transmembrane helices of STX17. Based on these findings, we propose a model in which STX17 recruitment to mature autophagosomes is temporally regulated by a PI4P-driven change in the surface charge of autophagosomes.

Introduction

Macroautophagy (hereafter, autophagy) is a highly conserved process of intracellular degradation (*Mizushima and Levine*, 2020; *Soreng et al.*, 2018). Membrane cisternae (called isolation membranes or phagophores) elongate, bend, and engulf cytoplasmic components. Closure of the rim of the cup-shaped structures results in the formation of autophagosomes. Subsequently, the autophagosomes fuse with lysosomes to degrade their enclosed contents. Autophagosome–lysosome fusion is strictly regulated; lysosomes fuse with only fully closed autophagosomes. If lysosomes were to fuse with intermediate unclosed structures and their inner membrane is degraded, then harmful lysosomal enzymes would leak out into the cytosol. This temporal regulation of autophagosome–lysosome fusion is achieved in mammals by two mechanisms. One is the regulated translocation of the autophagosomal SNARE syntaxin 17 (STX17), which is recruited immediately before or after the closure of autophagosomes (*Itakura et al.*, 2012; *Takáts et al.*, 2013; *Tsuboyama et al.*, 2016). The other is the activation of YKT6, a conserved autophagosomal SNARE (*Matsui et al.*, 2018), which is kept inactivated by ULK1 (a homolog of yeast Atg1)-mediated phosphorylation until the completion of autophagosome formation (ULK1/Atg1 is dissociated at this time) (*Barz et al.*, 2020; *Gao et al.*, 2020; *Sanchez-Martin et al.*, 2023). Then, STX17 interacts with SNAP29 and the lysosomal SNARE protein VAMP7 or VAMP8, and YKT6 interacts with SNAP29 and the lysosomal STX7 to mediate the fusion between autophagosomes and lysosomes.

However, the molecular mechanism underlying the late recruitment of STX17 is not known. A previous study reported that LC3/GABARAP family proteins and immunity-related GTPase M (IRGM) are involved in autophagosomal recruitment of STX17 (*Kumar et al.*, 2018a), whereas other studies have shown that LC3/GABARAP family proteins are not required (*Nguyen et al.*, 2016; *Tsuboyama et al.*, 2016). It has also been recently reported that phosphorylation of STX17 and binding to filamin A are important for STX17 recruitment (*Wang et al.*, 2023). Although these factors may help STX17 recruitment, these mechanisms do not explain the strict temporal regulation of STX17 recruitment.

Accordingly, we hypothesized that there exists a yet unknown change in some

70 autophagosomal properties during maturation that is recognized by STX17. In this
71 study, we reveal that STX17 recruitment to autophagosomes requires positively charged
72 amino acids in the C-terminal region of STX17. Consistently, the membrane of
73 autophagosomes becomes more negatively charged when autophagosomes acquire
74 STX17. Furthermore, we show that phosphatidylinositol 4-phosphate (PI4P), a
75 negatively charged phospholipid, accumulates during autophagosome maturation and is
76 required for STX17 recruitment. Based on these findings, we propose a model in which
77 STX17 recruitment to mature autophagosomes is temporally regulated by the
78 electrostatic change of autophagosomes.
79

Results

Autophagosomal localization of STX17 requires a positively charged C-terminal region

STX17 has an N-terminal Habc domain, followed by a SNARE domain, two tandem transmembrane helices, and a short C-terminal region, with both N- and C-terminal ends facing the cytosol (Figure 1A) (*Itakura et al.*, 2012). A short construct containing only the transmembrane helices and the C-terminal region (STX17TM), which behaves similarly to full-length STX17 (*Itakura et al.*, 2012), colocalized with ring-shaped autophagosomes labeled with the general autophagic membrane marker microtubule-associated protein light chain 3B (LC3B) (Figure 1B and C). STX17 is a tail-anchored protein, and the C-terminal region of tail-anchored proteins is generally important for specific membrane targeting (*Rao et al.*, 2016; *Yagita et al.*, 2013). Therefore, we determined the role of the C-terminal region of STX17. In the following experiments, we used the STX17TM construct in order to avoid detecting an indirect effect of SNARE domain-mediated translocation. Deletion of the C-terminal cytosolic region from STX17TM (TMΔC) resulted in a diffuse cytosolic pattern (Figure 1C), indicating that not only the transmembrane helices but also the C-terminal region of STX17 are required for its proper autophagosomal localization. Although the role of STX17 in autophagosome–lysosome fusion is conserved in both *Drosophila melanogaster* (Dm) (*Takáts et al.*, 2013) and *Caenorhabditis elegans* (Ce) (*Guo et al.*, 2014), the amino acid sequence of the C-terminal region is not conserved in these organisms (Figure 1—figure supplement 1A). Nevertheless, when expressed in mammalian cells, DmSTX17TM and CeSTX17TM were recruited to autophagosomes, although less efficiently (Figure 1—figure supplement 1B), suggesting that recruitment of STX17 does not depend on the specific amino acid sequence in the C-terminal region.

In general, cationic amino acids in the C-terminal region of tail-anchored proteins are important for targeting membranes (*Borgese et al.*, 2001; *Horie et al.*, 2002; *Yagita et al.*, 2013). STX17 has cationic amino acids in its C-terminal region, and the replacement of lysine and arginine with alanine impaired autophagosomal localization in a dose-dependent manner (Figure 1A and D, Figure 1—figure supplement 1C).

111 Moreover, the replacement of the C-terminal region with artificial sequences consisting
112 of five residues of positively charged lysine or arginine, but not negatively charged
113 aspartic acid or uncharged alanine, restored the localization of STX17 to
114 autophagosomes (Figure 1E, Figure 1—figure supplement 1D). These data suggest that
115 autophagosomal localization of STX17 requires positively charged residues, but not
116 sequence-specific structures, in its C-terminal region.
117
118 **The membrane of autophagosomes becomes negatively charged during maturation**
119 Given the importance of positively charged residues in the C-terminal region, we
120 hypothesized that STX17 favors negatively charged membranes. To evaluate this
121 hypothesis, we first conducted an *in vitro* membrane binding assay using liposomes with
122 different compositions of phospholipids. STX17TM was efficiently recruited to
123 liposomes containing anionic phospholipids such as phosphatidylserine (PS),
124 phosphatidylinositol (PI) 3-phosphate (PI3P) or PI4P (Figure 2A). The association of
125 STX17TM with PI4P-containing membranes was abolished in the presence of 1 M
126 NaCl (Figure 2B). These data suggest that STX17 can be recruited to negatively
127 charged membranes via electrostatic interaction independent of the specific lipid
128 species.
129 Next, we tested whether autophagosomal membranes are indeed negatively
130 charged. To monitor membrane charge *in vivo*, we used membrane surface charge
131 biosensors (Figure 2C) (*Simon et al.*, 2016; *Yeung et al.*, 2006). These surface charge
132 probes have a diverse range of positively charged peptides and a farnesylated anchor at
133 their C terminus, with GFP fused to their N terminus. The name of each probe is
134 indicated by the number of lysine (positively charged) followed by that of glutamine.
135 The probe for the most negatively charged membrane (9K0Q) labeled the plasma
136 membrane, which is known to have a highly negative charge (*Li et al.*, 2014), but not
137 autophagosomes (Figure 2D and E, Figure 2—figure supplement 1A). However, the
138 probes for intermediate (5K4Q and 3K6Q) and weakly (1K8Q) negative charges labeled
139 not only the plasma membrane but also LC3B- and STX17-positive autophagosomes
140 (Figure 2D and E, Figure 2—figure supplement 1A). The recruitment kinetics differed
141 between the intermediate and weakly negative charge probes. The 1K8Q probe was

recruited to not only STX17-positive spherical autophagosomes but also STX17-negative, LC3B-positive elliptic structures that should correspond to unclosed autophagosomes (*Tsuboyama et al.*, 2016) (Figure 2F). In contrast, the intermediate charge probes (3K6Q and 5K4Q) were recruited to spherical LC3B-positive autophagosomes at almost the same time as STX17 (Figure 2G, Figure 2—figure supplement 1B). Structures positive for ATG5, a marker for unclosed autophagosomes, were labeled with 1K8Q but not with 3K6Q or 5K4Q (Figure 2—figure supplement 1C). These results, which are summarized in Figure 2H, suggest that mature autophagosomes are more negatively charged compared with unclosed intermediate structures.

The accumulation of PI4P in mature autophagosomes coincides with STX17 recruitment

We next explored the mechanism that generates the negative charges of autophagosomal membranes. As the change in the membrane charge was rapid and robust, we reasoned that it could be caused by a change in lipid composition or modification. We screened negatively charged lipids that are enriched in autophagosomal membranes using various phospholipid probes (*Platre and Jaillais*, 2016). Among them, we found that the probes for PI4P (GFP-fused PH domain of CERT; GFP–CERT(PHD) and phosphatidylinositol 3,5-bisphosphate (PI(3,5)P_2) (GFP–TRPML1(PHD)) colocalized with STX17-positive ring-shaped structures (Figure 3—figure supplement 1A). Since PI(3,5)P_2 was primarily present in lysosomes (Figure 3—figure supplement 1B) (*Dong et al.*, 2010), PI(3,5)P_2 enrichment likely occurs after fusion with lysosomes. The CERT(PHD) (W33A) mutant, lacking PI4P-binding activity, was not co-localized with STX17TM (Figure 3–figure supplement 2A) (*Sugiki et al.*, 2012). Consistently, other PI4P probes, including FAPP(PHD), OSBP(PHD), and P4M-SidMx2, colocalized with STX17TM (Figure 3—figure supplement 2B and C) (*Hammond et al.*, 2014; *Platre and Jaillais*, 2016).

PI4P is an important lipid component of the Golgi complex and the plasma membrane as well as a major regulator of conserved eukaryotic cellular processes (*Balla*, 2013; *Platre et al.*, 2018; *Schink et al.*, 2016). In the context of autophagy, it was previously reported that GABARAP-dependent PI4P production by PI4K2A (PI4KIIα)

173 is required for autophagosome–lysosome fusion (*Wang et al.*, 2015), and that PI4KB
174 (PI4KIIIβ) is detected in ATG9A vesicles and early autophagic structures and is
175 furthermore required for autophagosome formation (*Judith et al.*, 2019). Consistently,
176 we detected faint signals of PI4K2A and PI4KB on LC3B-positive structures (Figure
177 3—figure supplement 1C). However, the dynamics of PI4P production during
178 autophagosome maturation has not been systematically determined.
179 The PI4P probes (CERT(PHD), FAPP(PHD), OSBP(PHD), and P4M-SidMx2)
180 colocalized with STX17 but not with ATG5 (Figure 3A, Figure 3—figure supplement
181 2B and C), suggesting that PI4P accumulates in mature autophagosomes. We then
182 investigated the dynamics of PI4P enrichment by time-lapse microscopy. The signal of
183 the CERT(PHD) probe appeared on LC3B-positive membranes only after the
184 disappearance of the unclosed autophagosome markers ATG5 and WIPI2B (Figure 3B
185 and C) and almost at the same time as STX17 localized (Figure 3D). This was followed
186 by the appearance of LysoTracker signals (note that LysoTracker signals have been
187 previously observed to appear ring-shaped until inner membrane degradation
188 (*Tsuboyama et al.*, 2016)) (Figure 3—figure supplement 2D). To confirm that PI4P
189 accumulation was independent of autophagosome–lysosome fusion, we evaluated the
190 colocalization among the PI4P probe, LC3B, and LAMP1 in STX17- and YKT6-
191 double-knockdown cells, in which unfused autophagosomes accumulated (*Matsui et al.*,
192 2018). The punctate structures of CERT(PHD) were still colocalized with LC3B-
193 positive and LAMP1-negative structures in these double-knockdown cells (Figure 3—
194 figure supplement 2E). In addition, STX17 recruitment and PI4P enrichment occurred
195 normally in cells lacking all ATG8 family proteins (LC3A, LC3B, LC3C, GABARAP,
196 GABARAPL1, and GABARAPL2) (Figure 3–figure supplement 2F). These results
197 suggest that PI4P accumulates in mature autophagosomal membranes independent of
198 lysosome fusion and ATG8 proteins, and that the kinetics of the accumulation of
199 STX17, the PI4P probes, and the negative charge probes are correlated.
200
201 **STX17 recruitment to autophagosomes depends on PI4P**
202 To determine whether PI4P is required for the recruitment of STX17 to
203 autophagosomes, we first tried to dephosphorylate PI4P by ectopic expression of SAC1,

204 a PI4P-phosphatase, on autophagosomes (*Manford et al.*, 2010). To this end, we fused
205 the phosphatase domain of yeast Sac1 (Sac1PD) to the N terminus of LC3B and
206 expressed them in different cell lines, using several methods, including lipofection and
207 retrovirus- and adenovirus-mediated transfection. Although Sac1PD–LC3B localized to
208 autophagosomes, it did not reduce either the level of autophagosomal PI4P or STX17
209 recruitment (unpublished observation). High expression of Sac1PD–LC3B inhibited
210 autophagosome formation (unpublished observation). Mammals possess four PI 4-
211 kinases. We next tried to deplete each or combinations of these PI 4-kinases by using
212 siRNA or an auxin-inducible degron system (*Yesbolatova et al.*, 2020) or inhibit them
213 using PI 4-kinase inhibitors, including PI-273 (*Li et al.*, 2017), BF738735 (unpublished
214 observation) (*van der Schaar et al.*, 2013), and NC03 (Figure 4—figure supplement 1)
215 (*Sengupta et al.*, 2019), but ultimately failed to reduce the autophagosomal PI4P levels
216 and STX17 recruitment. Although the precise reason for this failure was not known,
217 these approaches were insufficient to deplete autophagosomal PI4P *in vivo*.
218 Therefore, we instead used an *in vitro* system to determine whether PI4P is
219 important for STX17 recruitment to autophagosomes (Figure 4A). Mature
220 autophagosomes prior to fusion with lysosomes were isolated from *STX17* knockout
221 (KO) cells (Figure 4B, Fraction #1) (*Matsui et al.*, 2018). Recombinant Sac1PD, its
222 phosphatase-dead mutant (C392S), and mGFP–STX17TM were generated using insect
223 cells (Figure 4C). Autophagosomes were first incubated with or without Sac1PD or
224 Sac1PD (C392S) for 30 min and then further incubated with mGFP–STX17TM for
225 another 30 min. Recombinant mGFP–STX17TM was associated with autophagosomes,
226 but it was significantly impaired by treatment with Sac1PD. Phosphatase-dead Sac1PD
227 (C392S) showed no effect (Figure 4D). These data suggest that PI4P is important for
228 autophagosomal recruitment of STX17.
229 We further determined the effect of PI4P on the dynamics of STX17TM on a
230 membrane by performing a molecular dynamics simulation. We used all-atom models
231 for STX17TM and the highly mobile membrane-mimetic (HMMM) model for the lipid
232 bilayer (*Ohkubo et al.*, 2012). The structure of STX17TM was predicted by trRosetta
233 (*Du et al.*, 2021), yielding five different models, all of which were used in the
234 simulation. The initial configuration was prepared such that the center of mass of

STX17TM was located 3 nm above the membrane surface, after which the movement of STX17TM was tracked. In independent simulations using four out of the five predicted STX17TM structures, STX17TM was inserted into the membrane with PI4P (PC:PE:PI4P = 70:20:10) within a short time scale of 100 ns (Figure 5A, B, Video 1). The two transmembrane helices were inserted into the membrane, while the charged C-terminal region remained bound to the membrane surface (Video 1). In contrast, STX17 diffused freely in the solution and was not inserted into the membrane without PI4P (PC:PE = 70:30) in simulations of all five structures (Figure 5C, D, Video 2). Moreover, if the membrane contained PI instead of PI4P, STX17TM approached the PI-containing membrane but was not inserted into the membrane (Figure 5E, F, Video 3). These results suggest that STX17TM can be readily inserted into PI4P-containing membranes.

Discussion

Based on the results of this study, we propose a model in which temporally regulated autophagosome–lysosome fusion involves a dynamic change in electrostatic status during autophagosome maturation; the recruitment of STX17 to mature autophagosomes is primarily mediated by the electrostatic interaction between the positively charged C-terminal region of STX17 and negatively charged autophagosomal membranes likely due to accumulation of PI4P (Figure 5G). During revising this manuscript, Juhász's group also reached a consistent model that PI4P is required for autophagosomal localization of STX17 (*Laczkó-Dobos et al.*, 2024). Because STX17 does not localize to all negatively charged membranes (e.g., the plasma membrane), the transmembrane helices appear to also regulate the specificity of target membranes. This is consistent with the "coincidence detector" mechanism in which both a cationic motif and a nearby membrane-anchored moiety are important for membrane targeting (*Carlton and Cullen*, 2005; *Yeung and Grinstein*, 2007).

A striking finding of this study is that the membrane of autophagosomes become more negatively charged during maturation, most likely through an increase in the PI4P content of their membranes, although we do not exclude the possible involvement of other negatively charged molecules. Given the possibility that fluorescence lipid probes may give false-negative results, a more comprehensive biochemical analysis, such as lipidomics analysis of mature autophagosomes, would be imperative to elucidate the potential involvement of other negatively charged lipids. While PI3P is important for autophagosome formation, we do not think that PI3P contributes to the increase in negative charge. It was reported that PI3P is dephosphorylated to PI during autophagosome formation or maturation (*Allen et al.*, 2020; *Cebollero et al.*, 2012; *Taguchi-Atarashi et al.*, 2010), and that the PI3P effectors DFCP1 and WIPI family proteins are not detected on mature autophagosomes (*Koyama-Honda et al.*, 2013). In fact, we did not detect WIPI2B and the PI3P reporter GFP–2×FYVE on PI4P-enriched structures (Figure 3C) and STX17-positive structures (Figure 3—figure supplement 1A), respectively. Considering the change in autophagosomal membrane charge, the amount of PI4P produced during

278 autophagosome maturation is likely to be higher than that of PI3P in the early stages.
279 Our data of the 1K8Q probe suggest that immature autophagosomal membranes may
280 also have slight negative charges (Figure 2F). Although the source of the negative
281 charge of immature autophagosomes is currently unknown, it may be derived from low
282 levels of PI4P, which is undetectable by the PI4P probes and/or other negatively charged
283 lipids such as PI and PS (*Schmitt et al.*, 2022).

284 PI4P is involved in many cellular processes, including autophagosome
285 formation and maturation. It was reported that PI4KB regulates the early stage of
286 autophagosome formation through interaction with ATG9A (*Judith et al.*, 2019). It was
287 also reported that PI4K2A is recruited to autophagosomes by binding to the ATG8
288 family proteins GABARAP and GABARAPL1 and produces PI4P in the
289 autophagosomal membranes (*Wang et al.*, 2015). Furthermore, the knockdown of
290 PI4K2A resulted in the accumulation of abnormally enlarged autophagosomes,
291 presumably owing to a defect in autophagosome–lysosome fusion (*Wang et al.*, 2015).
292 Indeed, a freeze-fracture replica labeling study showed that autophagosomal membranes
293 contain PI4P in the cytoplasmic leaflets of the outer and inner membranes (*Kurokawa et*
294 *al.*, 2019). Very recently, it was reported that the knockdown of PI4KIIα in *Drosophila*
295 blocked autophagic flux at a late step of autophagy in the fat body (*Liu et al.*, 2023).
296 Although these studies are consistent with our finding that PI4P production induces
297 STX17 recruitment for fusion with lysosomes, our repeated attempts to deplete PI4P
298 genetically (i.e., by depletion of PI 4-kinases or attachment of Sac1 to autophagosomes)
299 or pharmacologically did not deplete autophagosomal PI4P or inhibit STX17
300 recruitment. Liu et al. also showed that the knockdown of PI4KIIα in *Drosophila* did
301 not inhibit STX17 recruitment. This may be because PI 4-kinases function redundantly.
302 In any case, it would be important to elucidate how PI 4-kinase activity or PI4P
303 synthesis is upregulated during autophagosome maturation.

304 Surface charge, which is now recognized as one of the key physical properties
305 of cellular membranes, regulates various biological processes (*Yeung and Grinstein*,
306 2007). For example, the negatively charged plasma membrane, where anionic
307 phospholipids such as PI(4,5)P_2 and PS are enriched, recruits positively charged
308 proteins, including K-Ras and Rac1 (*Bigay and Antonny*, 2012; *Heo et al.*, 2006; *Li et*

309 *al.*, 2014; *Platre et al.*, 2018; *Yeung et al.*, 2008; *Yeung et al.*, 2006), some of which are
310 released from the membrane when the negative charge of the surface is reduced during
311 phagocytosis (*Yeung et al.*, 2006). However, little has been reported on the role of
312 electrostatic properties of other organelles, including autophagosomes.
313 Generally, PI4P can be structurally recognized by a series of PI4P-binding
314 domain-containing proteins (*Lemmon*, 2008; *Moravcevic et al.*, 2012). However, recent
315 studies suggest that PI4P can also generate a negatively charged electrostatic field and
316 recruit positively charged proteins independent of specific amino acid motifs
317 (*Hammond et al.*, 2012; *Simon et al.*, 2016). Examples of the role of PI4P in
318 electrostatic signature include the recruitment of the polar auxin transport regulator
319 PINOID and other signaling molecules to the cell plate in plants (*Simon et al.*, 2016);
320 the recruitment of D6 protein kinase (*Barbosa et al.*, 2016), NPH3 (*Reuter et al.*, 2021),
321 and the exocyst complex (*Synek et al.*, 2021) to the plasma membrane in plants; the
322 recruitment of Lgl and Dlg proteins, which function in cell polarity and tumorigenesis,
323 to the plasma membrane in *Drosophila* (*Dong et al.*, 2015; *Lu et al.*, 2021); and the
324 recruitment of NLRP3 to the disassembled trans-Golgi network during inflammasome
325 activation in mammals (*Chen and Chen*, 2018). In the present study, we showed that
326 autophagosomal PI4P also serves as a regulator of surface charge. Given that the
327 function of elongating unclosed autophagosomes (i.e., sequestration) and mature closed
328 autophagosomes (i.e., fusion with lysosomes) differs despite using seemingly the same
329 membrane, electrostatic maturation would be an efficient way for the function to switch.
330
331

Materials and Methods

Plasmids and antibodies

First, cDNAs encoding human STX17 (*Itakura et al.*, 2012), *D. melanogaster* STX17 (NM_079202), *C. elegans* STX17 (NM_059941), rat LC3B (*Hara et al.*, 2008), and mouse ATG5 (NM_053069) were inserted into pMRXIP (harboring a puromycin-resistant marker) (*Kitamura et al.*, 2003; *Saitoh et al.*, 2002), pMRXIZ (harboring a zeocin-resistant marker) (*Morita et al.*, 2018), and pMRXIB (harboring a blasticidin-resistant marker) (*Morita et al.*, 2018) together with enhanced GFP or mRuby3 (codon-optimized, Addgene #74252). STX17 fragments and their point mutations were generated by a standard PCR method or PCR-mediated site-directed mutagenesis.

Membrane surface charge probes were constructed by annealing with the following oligonucleotides (purchased from Thermo Fisher Scientific), after which they were inserted into pMRXIP plasmid with enhanced GFP:

GFP–9K0Q (GGCTCGGGATCCGGGAATTCATCCAAAGATGGAAAAAAAAAGAAGAAGAAAAGTAAAACCAAATGCGTGATTATGTAACTCGAGAGCGGCCGCT, AGCGGCCGCTCTCGAGTTACATAATCACGCATTTGGTTTTACTTTTCTTCTTCTTTTTTTTCCATCTTTGGATGAATTCCCGGATCCCGAGCC); GFP–5K4Q (GGCTCGGGATCCGGGAATTCAAGCAAAGACGGCCAGCAGCAACAAAAGAAGTCTAAGACCAAGTGTGTAATCATGTAACTCGAGAGCGGCCGCT, AGCGGCCGCTCTCGAGTTACATGATTACACACTTGGTCTTAGACTTCTTTTGTTGCTGCTGGCCGTCTTTGCTTGAATTCCCGGATCCCGAGCC); GFP–3K6Q (GGCTCGGGATCCGGGAATTCATCCAAGGACGGACAACAGCAGCAACAACAGAGTAAAACTAAATGCGTGATAATGTAACTCGAGAGCGGCCGCT, AGCGGCCGCTCTCGAGTTACATTATCACGCATTTAGTTTTACTCTGTTGTTGCTGCTGTTGTCCGTCCTTGGATGAATTCCCGGATCCCGAGCC); GFP–1K8Q (GGCTCGGGATCCGGGAATTCATCCCAGGACGGTCAGCAGCAACAACAGCAATCACAAACTAAATGTGTAATAATGTAACTCGAGAGCGGCCGCT, AGCGGCCGCTCTCGAGTTACATTATTACACATTTAGTTTGTGATTGCTGTTGTTGCTGCTGACCGTCCTGGGATGAATTCCCGGATCCCGAGCC). GFP-0K9Q was

363 generated by PCR-mediated site-directed mutagenesis.

364 To generate lipid probes, cDNAs encoding human 2×Spo20(PABD)
365 (NM_005633; amino acids 422–551) (*Kassas et al.*, 2017), CERT(PHD)
366 (NM_001130105; amino acids 1–116) (*Hanada*, 2006), FAPP (NM_001807; amino
367 acids 1–101) (*Balla et al.*, 2005), OSBP (NM_002556; amino acids 87–185) (*Levine*
368 *and Munro*, 1998), 2×ING2(PlantHD) (NM_001564; amino acids 190–280) (*Gozani et*
369 *al.*, 2003), 2×TAPP1(PHD) (NM_001001974; amino acids 184–304) (*Dowler et al.*,
370 2000), 2×TRPML1(PHD) (NM_020533; amino acids 1–69) (*Dong et al.*, 2010), Btk
371 (NM_000061; amino acids 1–177) (*Baraldi et al.*, 1999), and rat PLCd1 (NM_017035;
372 amino acids 1–175) (*Varnai and Balla*, 1998) were inserted into pMRXIP. GFP–
373 Evectin-2 was provided by Hiroyuki Arai; GFP–PKD C1ab was provided by Tamas
374 Balla; and mRFP–2×FYVE was provided by Harald Stenmark. GFP–P4M-SidMx2
375 (51472; Addgene) was amplified by PCR and subcloned into pMRXIP.

376 For the *in vitro* autophagosome recruitment assay, DNA fragments encoding
377 GST–HRV3C-tagged yeast Sac1 (phosphatase domain; 2–517 amino acids)
378 (NM_001179777) or its C392S mutant and mGFP (monomeric enhanced GFP with
379 A206K mutation)–STX17TM were inserted downstream of the polyhedrin promoter of
380 the pFastBac Dual Expression vector (10712024; Thermo Fisher Scientific).

381 For immunoblotting, mouse monoclonal anti-TOMM20 (sc-11415; Santa Cruz
382 Biotechnology, Inc.), rabbit polyclonal anti-LAMP1 (ab24170; Abcam), anti-p62
383 (PM045; MBL), and anti-LC3B (*Kabeya et al.*, 2000) antibodies were used as primary
384 antibodies. HRP-conjugated anti-mouse IgG and HRP-conjugated anti-rabbit IgG (111-
385 035-003, 111-035-144; Jackson ImmunoResearch Laboratories) antibodies were used as
386 secondary antibodies.

387 For immunostaining, rabbit polyclonal anti-LAMP1 (ab24170; Abcam) was
388 used as a primary antibody, while Alexa Fluor 660-anti-rabbit IgG (A-21074; Molecular
389 Probes) was used as secondary antibodies.

390

391 **Cell culture**

392 Mouse embryonic fibroblasts (MEFs), U2OS cells, HeLa cells, and human embryonic
393 kidney (HEK) 293T cells were cultured in Dulbecco's modified Eagle's medium

394 (DMEM) (D6546; Sigma-Aldrich) supplemented with 10% fetal bovine serum (FBS)
395 (S1820500; Biowest) and 2 mM L-glutamine (25030081; Gibco) in a 5% CO_2 incubator.
396 For the starvation treatment, cells were washed twice with phosphate-buffered saline
397 (PBS) and incubated in amino acid-free DMEM (04833575; Fujifilm Wako Pure
398 Chemical Corp.) without FBS. The *STX17* KO HeLa cells used in the present study
399 were as previously described (*Matsui et al.*, 2018). ATG8 hexa KO HeLa cells (lacking
400 LC3A, LC3B, LC3C, GABARAP, GABARAPL1, and GABARAPL2) were kindly
401 provided by Michael Lazarou (*Nguyen et al.*, 2016).
402 For transient expression of mRuby3–CERT(PHD), HeLa cells were transiently
403 transfected using FuGENE HD (VPE2311; Promega) with pMRXIB-mRuby3–
404 CERT(PHD) for 24 h in Opti-MEM (31985-070; Gibco).
405
406 **Retroviral infections and generation of stable cell lines**
407 HEK293T cells were transiently transfected using Lipofectamine 2000 (11668019;
408 Thermo Fisher Scientific) or FuGENE HD (VPE2311; Promega) with retrovirus
409 vectors, pCG-gag-pol, and pCG-VSV-G (provided by Teruhiko Yasui). After cells were
410 cultured for 2–3 days, the supernatant was collected and filtered through a 0.45-μm
411 syringe filter unit (SLHV033RB; EMD Millipore). The obtained cells were cultured
412 with retrovirus and 8 μg/ml polybrane (H9268; Sigma-Aldrich). Uninfected cells were
413 eliminated by puromycin (P8833; Sigma-Aldrich), blasticidin (02218713; Fujifilm
414 Wako Pure Chemical Corp.), geneticin (10131; Thermo Fisher Scientific), and zeocin
415 (R25005; Thermo Fisher Scientific).
416
417 **Fluorescence microscopy**
418 Live-cell fluorescence imaging was performed using a Delta Vision Elite widefield
419 fluorescence microscope (GE Healthcare Life Science) equipped with a 100× PlanAPO
420 oil-immersion objective lens (Olympus, NA1.40) and a cooled-CCD camera
421 (Photometrics, CoolSNAP HQ2). Cells stably expressing GFP and mRuby3 were grown
422 on a glass-bottom dish (617870; Greiner bio-one, or 11004006; IWAKI). To observe
423 lysosomes, 50 nM Lysotracker Red DND99 (L7528; Thermo Fisher Scientific) or
424 LysoTracker Deep Red (L12492; Thermo Fisher Scientific) was added to the medium.

425 To observe HaloTag–LC3B, cells were observed in the presence of 200 nM SaraFluor
426 650T HaloTag ligand (GoryoChemical, A308-02). During live-cell imaging, the culture
427 dish was mounted in a chamber (INUB-ONI-F2; TOKAI HIT) to maintain the culture
428 conditions (37°C, 5% CO_2). Images were acquired at 30-s intervals. Time series of 16-
429 bit images were converted into RGB Tiff images using ImageJ software (Rasband, W.S.,
430 ImageJ, U. S. National Institutes of Health, http://imagej.nih.gov/ij/, 1997–2018). GFP
431 intensity of autophagosomal structures was determined using ImageJ. Additionally,
432 mRuby3–LC3 or Atg5-positive structures, including punctate and cup-shape structures
433 (premature autophagosomes) and ring-like structures (mature autophagosomes) were
434 extracted by the Analyze Particle function after binarization using the Auto Threshold
435 v1.17 plugin (Method, Max Entropy). The GFP intensity of each particle was measured
436 by the Measure ImageJ plugin, and the background signal (i.e., average GFP intensity of
437 the entire cell) was subtracted.
438 The GFP–STX17TM intensity of mature autophagosomes or liposomes was
439 determined using ImageJ. The center of ring-like structures in the red channel (LC3B or
440 liposome signals) was first selected using the multi-point tool. The region of interest
441 (ROI) was then defined by drawing a 10-μm-diameter circle around the previously
442 determined center and capturing the red channel (LC3B or liposome signals). The GFP–
443 STX17TM intensity was measured by the Radial Profile Plot ImageJ plugin, and the
444 background signal of the surrounding cytosol area was subtracted.
445
446 **Preparation of recombinant proteins**
447 *In vitro* transcription and translation in the rabbit reticulocyte lysate system were
448 performed according to a published method with minor modifications (*Sharma et al.*,
449 2010). For *in vitro* mRNA synthesis, DNA templates containing the SP6 RNA
450 polymerase promoter site upstream of the sequence to be transcribed were generated by
451 a standard PCR method and then incubated for 1 h at 37°C using the mMACHINE SP6
452 Transcription Kit (AM1340; Thermo Fisher Scientific). For *in vitro* protein synthesis,
453 transcripts were incubated with rabbit reticulocyte lysates (L4960; Promega) for 30 min
454 at 37°C.
455 Recombinant yeast Sac1 (amino acids 2–517) and mGFP–STX17TM (amino

456 acids 229–302) proteins were prepared using the Bac-to-Bac baculovirus expression
457 system (10359016; Thermo Fisher Scientific). Bacmid DNAs were prepared using
458 DH10Bac *E. coli* cells (10361012; Thermo Fisher Scientific), after which High Five
459 insect cells (BTI-TN-5B1-4; B85502; Thermo Fisher Scientific) were transfected with
460 the bacmid DNAs using Cellfectin II (10362100; Thermo Fisher Scientific).
461 Baculoviruses were generated and amplified in the High Five cells. After a 96-h viral
462 infection, the cells were suspended in 2 ml of ice-cold homogenization buffer (20 mM
463 HEPES-KOH, pH 7.2, 250 mM sucrose, 1 mM EDTA, and protease inhibitor cocktail).
464 Cells were then disrupted by ultrasonication using a UD-201 ultrasonic disruptor
465 (TOMY). After centrifugation at 16,500 × *g* for 10 min, the supernatants were incubated
466 with Glutathione Sepharose 4B (17075601; GE Healthcare) for 3 h at 4°C with gentle
467 rotation. The sepharose resins were washed three times with homogenization buffer and
468 then treated with HRV3C protease (206-18151; Fujifilm Wako Pure Chemical Corp.) for
469 12 h at 16°C. The eluted proteins were stored at −80°C. To confirm recombinant
470 expression, purified samples were separated by SDS-PAGE and detected by CBB
471 staining using CBB Stain One Super (11642-31; Nacalai Tesque).
472
473 **Preparation of phospholipid vesicles**
474 Liposomes were prepared as follows. First, 1,2-dioleoyl-sn-glycero-3-phosphocholine
475 (DOPC) (850375 C; Avanti Polar Lipids), 1,2-dioleoyl-sn-glycero-3-
476 phosphoethanolamine (DOPE) (850725 C; Avanti Polar Lipids), 1,2-dioleoyl-sn-
477 glycero-3-phospho-L-serine (DOPS) (840035P; Avanti Polar Lipids), 1,2-dioleoyl-sn-
478 glycero-3-phospho-(1′-myo-inositol) (18:1 PI) (850149P; Avanti Polar Lipids), 1,2-
479 dioleoyl-sn-glycero-3-phospho-(1′-myo-inositol-3′-phosphate) (18:1 PI3P) (850150P;
480 Avanti Polar Lipids), 1,2-dioleoyl-sn-glycero-3-phospho-(1′-myo-inositol-4′-phosphate)
481 (18:1 PI4P) (850151P; Avanti Polar Lipids), and 1,2-dioleoyl-sn-glycero-3-phospho-(1′-
482 myo-inositol-3′,4′-bisphosphate) (18:1 PI(3,4)P_2) (850153P; Avanti Polar Lipids)
483 dissolved in chloroform to 1 μM final concentrations were mixed in a glass tube at the
484 indicated ratios in the figure legends. Then, 1,2-distearoyl-sn-glycero-3-
485 phosphoethanolamine-*N*-[biotinyl(polyethylene glycol)-2000] (DSPE-PEG(2000)
486 Biotin) (880129C; Avanti Polar Lipids) and 1,2-dioleoyl-sn-glycero-3-

487 phosphoethanolamine-*N*-(lissamine rhodamine B sulfonyl) (18:1 Liss Phod PE)
488 (810150C; Avanti Polar Lipids) were added to the mixtures to label the liposomes. The
489 chloroform was evaporated under argon gas and then completely dried in a vacuum
490 desiccator overnight. The lipid film was hydrated in KHM buffer (20 mM HEPES-
491 NaOH [pH 7.4], 110 mM potassium acetate, 2 mM $MgCl_2$) at a concentration of 1 mM
492 and incubated for 16 h at 30°C.
493
494 **Purification of mature autophagosomes**
495 *STX17* KO HeLa cells stably expressing mRuby3–LC3B were harvested from two 10-
496 cm dishes and washed twice with ice-cold PBS. The cell pellets were collected after
497 centrifugation at 700 × *g* for 5 min and resuspended in 1 ml of ice-cold homogenization
498 buffer (20 mM HEPES-KOH, pH7.2, 250 mM sucrose, 1 mM EDTA, and protease
499 inhibitor cocktail). Cells were then disrupted by passage through a 25-gauge needle. The
500 homogenized cells were centrifuged at 3,000 × *g* for 10 min to remove cell debris and
501 undisrupted cells. The supernatant was diluted with an equal volume of 50% OptiPrep
502 (1893; Cosmo Bio) with complete EDTA-free protease inhibitor (11873580001; Roche).
503 Discontinuous OptiPrep gradients were generated in MLS-50 tubes (344057; Beckman
504 Coulter) by overlaying each of the following OptiPrep solutions in homogenization
505 buffer (20 mM HEPES-KOH [pH 7.4], 250 mM sucrose, 1 mM EDTA): 1.25 ml of the
506 diluted supernatant in 25% OptiPrep, 0.25 ml in 20%, 0.75 ml in 15%, 0.75 ml in 10%,
507 2.0 ml in 5%, and 0.25 ml in 0%. The gradients were centrifuged at 150,000 × *g* in
508 MLS-50 rotors (Beckman Instruments) for 3 h, and subsequently, 10 fractions (0.5 ml
509 each) were collected from the top. Proteins in each fraction were isolated by TCA
510 precipitation. The samples were separated by SDS-PAGE and transferred to Immobilon-
511 P polyvinylidene difluoride membranes (IPVH00010; EMD Millipore). Immunoblotting
512 analysis was performed with the indicated antibodies. Immobilon Western
513 Chemiluminescent HRP Substrate (P90715; EMD Millipore) was used to visualize the
514 signals, which were detected on an IQ800 biomolecular imager (Cytiva). Contrast and
515 brightness adjustments were performed using Photoshop 2022 (Adobe).
516
517 ***In vitro* recruitment assay**

518 For the liposome binding assay, the prepared liposomes were mixed with recombinant
519 proteins produced by rabbit reticulocyte lysate for 15 min at 30°C. A 0.2-mm-thick
520 chamber was created by attaching two glass cover slips (Matunami glass) together with
521 double-sided tape applied along the long edges. NeutrAvidin Protein (31000; Thermo
522 Fisher Scientific) was added to the chamber for 15 min at room temperature before
523 being washed out with KHM buffer. The liposome–recombinant protein mixture was
524 then transferred to the NeutrAvidin Protein-coated chamber. Images were captured
525 immediately after using a confocal microscope (FV3000; Olympus) equipped with a
526 60× PlanAPO oil-immersion objective lens (Olympus, NA1.42).
527 For the autophagosome recruitment assay, the LC3-positive, LAMP1-negative
528 autophagosomal fraction was incubated with 0.5 μg of Sac1 proteins from insect cells
529 for 30 min at 37°C. Then, mGFP–STX17TM was added to the mixture, which was then
530 incubated again for 30 min at 37°C. The mixtures were transferred to a glass-bottom
531 dish (617870; Greiner bio-one), and images were captured using a fluorescence
532 microscope (BZ-810; Keyence) equipped with a 60× oil-immersion objective lens
533 (Nikon, NA1.40).
534
535 **RNA interference**
536 Stealth RNAi oligonucleotides were purchased from Thermo Fisher Scientific. The
537 following sequences were used: human YKT6 siRNA antisense, 5′-
538 GGTGTGGTCATTGCTGACAATGAAT -3′; human YKT6 siRNA antisense sense, 5′-
539 ATTCATTGTCAGCAATGACCACACC -3′ (*Matsui et al.*, 2018). The siRNA
540 oligonucleotides for human STX17 (HSS123732 antisense, 5′-
541 AATTAAGTCCGCTTCTAAGGTTTCC -3′; HSS123732 sense, 5’-
542 GGAAACCTTAGAAGCGGACTTAATT -3′) were previously reported (*Itakura et al.*,
543 2012). The stealth RNAi oligonucleotides were transfected into cells using
544 Lipofectamine RNAiMAX (13778150; Thermo Fisher Scientific) according to the
545 manufacturer’s instructions. Three days after transfection, cells were used for analysis.
546
547 **Immunostaining**
548 Cells grown on coverslips were washed with PBS and fixed with 4% paraformaldehyde

549 phosphate buffer solution (0915485; Nacalai Tesque) for 10 min at room temperature.
550 Fixed cells were permeabilized with 50 μg/ml digitonin (D141; Sigma-Aldrich) in PBS
551 for 5 min, blocked with 3% BSA in PBS for 10 min, and then incubated with primary
552 antibodies for 16 h at 4°C. After being washed three times with PBS, cells were
553 incubated with secondary antibodies for 1 h at room temperature. The coverslips were
554 observed using a confocal laser microscope (FV3000; Olympus) equipped with a 60×
555 PlanAPO oil-immersion objective lens (Olympus, NA1.42).
556
557 **Sequence alignment**
558 Amino acid sequences of STX17 from the following species were obtained from the
559 NCBI protein database: *Homo sapiens* (NP_060389.2), *Mus musculus* (NP_080619.2),
560 *Danio rerio* (NP_001007450.1), *Ciona intestinalis* (NP_492342.1), *Drosophila*
561 *melanogaster* (NP_523926.1), and *Caenorhabditis elegans* (NP_492342.1). The
562 sequences were aligned using clustal W (https://www.genome.jp/tools-bin/clustalw) as
563 implemented in Molecular Evolutionary Genetics Analysis X (*Kumar et al.*, 2018b).
564
565 **Molecular dynamics simulation**
566 We used the all-atom model for SXT17TM utilizing initial structures predicted by
567 trRosetta, a method based on deep learning (*Du et al.*, 2021). Because five different
568 three-dimensional structural models were predicted (TM score > 0.7), each was used in
569 the simulations. The lipid bilayer was modeled using the HMMM model, which was
570 developed to study protein–membrane interactions more efficiently by replacing the
571 membrane lipids with short-chain lipid and organic solvents to facilitate lateral diffusion
572 (*Ohkubo et al.*, 2012). The lipid headgroups in the HMMM model were identical to
573 those in the all-atom model and faithfully represented the membrane surface. The lipid
574 membrane consisted of 150 lipid molecules in each leaflet. The membranes with and
575 without PI4P were examined for lipid compositions of POPC:POPE:POPI4P (POPI14)
576 = 70:20:10, 70:30:0 or POPC:POPE:POPI = 70:20:10 respectively. The initial
577 configuration was prepared so that the center of mass of STX17TM was located 3 nm
578 above the membrane surface and the first principal axis of the atomic configuration was
579 tilted 45 degrees from the z axis. The protein and lipids were solvated in a 10 nm × 10

580 nm × 30 nm box with the TIP3P water model and 0.15 M KCl ions. The initial
581 configurations were built by the Membrane Builder module in the CHARMM-GUI
582 server (*Jo et al.*, 2008). All molecular dynamics simulations were performed using
583 GENESIS (*Jung et al.*, 2015). The CHARMM36 force-field was used to describe the
584 interactions in the system (*Huang et al.*, 2017). Energy minimization was performed for
585 1000 steps by the steepest descent algorithm and then by the conjugate gradient
586 algorithm. Then, a 250 ps NVT simulation was performed at 303.15 K for solvent
587 equilibration, followed by a 1.6 ns NPT equilibration to 1 atm using the Langevin
588 thermostat/barostat (*Quigley and Probert*, 2004). The production simulations were
589 performed for 100 ns with a time-step of 2.5 fs and the Langevin thermostat/barostat.
590 Long-range electrostatic interactions were simulated using the particle-mesh Ewald
591 method (*Darden et al.*, 1993; *Essmann et al.*, 1995). The short-range electrostatic and
592 van der Waals interactions both used a cutoff of 12 Å. All bonds were constrained by the
593 SHAKE/RATTLE algorithm (*Andersen*, 1983; *Ryckaert et al.*, 1977).
594
595 **Statistical analysis**
596 Comparisons between data from two groups were evaluated using Welch's *t*-test, and
597 comparisons of data among multiple groups were performed using one-way analysis of
598 variance (ANOVA) followed by the Dunnett's, Sidak's, or Tukey's multiple comparison
599 tests as implemented in GraphPad Prism 8 and 9 (GraphPad Software). Data
600 distributions were assumed to be normal, but this was not formally tested.
601
602 **Acknowledgments**
603 We thank Shoji Yamaoka for providing pMRX-IP vector, Teruhito Yasui for the pCG-
604 gag-pol and pCG-VSV-G vectors, Hiroyuki Arai for *C. elegans* cDNA and GFP–
605 Evectin-2, Masayuki Miura for *D. melanogaster* cDNA, Tamas Balla for GFP–PKD
606 C1ab, Harald Stenmark for mRFP–2xFYVE, Michael Lazarou for ATG8 hexa KO HeLa
607 cells, Yuji Sugita and Ai Niitsu for helpful discussions on the molecular dynamics
608 calculations, Koki Kamiya and Shoji Takeuchi for helping the liposome experiments,
609 and Gábor Juhász for helpful discussion and sharing his unpublished results. The
610 numerical computations were performed with the RIKEN supercomputer system

(HOKUSAI). We thank Eisuke Itakura for technical advice on the *in vitro* experiments. We thank the members of the Mizushima Laboratory for helpful discussions, especially Maya Shirakawa for technical assistance with the experiments. This work was supported by Grants-in-Aid for Specially Promoted Research (22H04919 to N.M.), for Transformative Research Areas (A) (21H05256 to H.Y.), for Scientific Research (C) (23K05715 to Y.S.), and for JSPS Fellows (17J02747 to S.S.) from the Japan Society for the Promotion of Science (JSPS) and by the Exploratory Research for Advanced Technology (ERATO) research funding program of the Japan Science and Technology Agency (JST) (JPMJER1702 to N.M.). The numerical computations were performed with the supercomputer systems at RIKEN (HOKUSAI, Fugaku) and the University of Tokyo (Wisteria/BDEC-01).

Author Contributions

S.S., H.Y., and N.M. designed the project and analyzed the data. S.S. performed most experimental work and analyzed data. Y.S. designed, performed, and analyzed the molecular dynamics simulation. S.S., T.M., M.U., and H.Y. performed *in vitro* reconstitution experiments. S.S., I.K.H., J.S., and H.Y. performed *in vivo* PI4P depletion analysis. S.S., Y.S., H.Y., and N.M. wrote the manuscript. H.Y. and N.M. supervised the project. All authors commented on the manuscript.

Competing Interest

Noboru Mizushima: a Reviewing editor, *eLife*. The other authors declare that no competing interests exist.

References

Allen, E.A., C. Amato, T.M. Fortier, P. Velentzas, W. Wood, and E.H. Baehrecke. 2020. A conserved myotubularin-related phosphatase regulates autophagy by maintaining autophagic flux. *J. Cell Biol.* **219**:e201909073. doi: 10.1083/jcb.201909073, PMID: 32915229

Andersen, H.C. 1983. Rattle: A “velocity” version of the shake algorithm for molecular dynamics calculations. *J. Comput. Phys.* **52**:24-34. doi: 10.1016/0021-9991(83)90014-1, PMID:

643 Balla, A., G. Tuymetova, A. Tsiomenko, P. Varnai, and T. Balla. 2005. A plasma
644 membrane pool of phosphatidylinositol 4-phosphate is generated by
645 phosphatidylinositol 4-kinase type-III alpha: studies with the PH domains of the
646 oxysterol binding protein and FAPP1. *Mol. Biol. Cell*. **16**:1282-1295. doi:
647 10.1091/mbc.e04-07-0578, PMID: 15635101
648 Balla, T. 2013. Phosphoinositides: tiny lipids with giant impact on cell regulation.
649 *Physiol. Rev.* **93**:1019-1137. doi: 10.1152/physrev.00028.2012, PMID: 23899561
650 Baraldi, E., K. Djinovic Carugo, M. Hyvonen, P.L. Surdo, A.M. Riley, B.V. Potter, R.
651 O'Brien, J.E. Ladbury, and M. Saraste. 1999. Structure of the PH domain from
652 Bruton's tyrosine kinase in complex with inositol 1,3,4,5-tetrakisphosphate.
653 *Structure*. **7**:449-460. doi: 10.1016/s0969-2126(99)80057-4, PMID: 10196129
654 Barbosa, I.C., H. Shikata, M. Zourelidou, M. Heilmann, I. Heilmann, and C.
655 Schwechheimer. 2016. Phospholipid composition and a polybasic motif
656 determine D6 PROTEIN KINASE polar association with the plasma membrane
657 and tropic responses. *Development*. **143**:4687-4700. doi: 10.1242/dev.137117,
658 PMID: 27836964
659 Barz, S., F. Kriegenburg, A. Henning, A. Bhattacharya, H. Mancilla, P. Sanchez-Martin,
660 and C. Kraft. 2020. Atg1 kinase regulates autophagosome-vacuole fusion by
661 controlling SNARE bundling. *EMBO Rep.* **21**:e51869. doi:
662 10.15252/embr.202051869, PMID: 33274589
663 Bigay, J., and B. Antonny. 2012. Curvature, lipid packing, and electrostatics of
664 membrane organelles: defining cellular territories in determining specificity.
665 *Dev. Cell*. **23**:886-895. doi: 10.1016/j.devcel.2012.10.009, PMID: 23153485
666 Borgese, N., I. Gazzoni, M. Barberi, S. Colombo, and E. Pedrazzini. 2001. Targeting of
667 a tail-anchored protein to endoplasmic reticulum and mitochondrial outer
668 membrane by independent but competing pathways. *Mol. Biol. Cell*. **12**:2482-
669 2496. doi: 10.1091/mbc.12.8.2482, PMID: 11514630
670 Carlton, J.G., and P.J. Cullen. 2005. Coincidence detection in phosphoinositide
671 signaling. *Trends Cell Biol.* **15**:540-547. doi: 10.1016/j.tcb.2005.08.005, PMID:
672 16139503
673 Cebollero, E., A. van der Vaart, M. Zhao, E. Rieter, D.J. Klionsky, J.B. Helms, and F.
674 Reggiori. 2012. Phosphatidylinositol-3-phosphate clearance plays a key role in
675 autophagosome completion. *Curr. Biol.* **22**:1545-1553. doi:
676 10.1016/j.cub.2012.06.029, PMID: 22771041
677 Chen, J., and Z.J. Chen. 2018. PtdIns4P on dispersed trans-Golgi network mediates
678 NLRP3 inflammasome activation. *Nature*. **564**:71-76. doi: 10.1038/s41586-018-

679 0761-3, PMID: 30487600
680 Darden, T., D. York, and L. Pedersen. 1993. Particle mesh Ewald: An $N \cdot \log(N)$ method
681 for Ewald sums in large systems. *J. Chem. Phys.* **98**:10089-10092. doi:
682 10.1063/1.464397, PMID:
683 Dong, W., X. Zhang, W. Liu, Y.J. Chen, J. Huang, E. Austin, A.M. Celotto, W.Z. Jiang,
684 M.J. Palladino, Y. Jiang, G.R. Hammond, and Y. Hong. 2015. A conserved
685 polybasic domain mediates plasma membrane targeting of Lgl and its regulation
686 by hypoxia. *J. Cell Biol.* **211**:273-286. doi: 10.1083/jcb.201503067, PMID:
687 26483556
688 Dong, X.P., D. Shen, X. Wang, T. Dawson, X. Li, Q. Zhang, X. Cheng, Y. Zhang, L.S.
689 Weisman, M. Delling, and H. Xu. 2010. PI(3,5)P_2 controls membrane trafficking
690 by direct activation of mucolipin Ca^{2+} release channels in the endolysosome.
691 *Nat. Commun.* **1**:38. doi: 10.1038/ncomms1037, PMID: 20802798
692 Dowler, S., R.A. Currie, D.G. Campbell, M. Deak, G. Kular, C.P. Downes, and D.R.
693 Alessi. 2000. Identification of pleckstrin-homology-domain-containing proteins
694 with novel phosphoinositide-binding specificities. *Biochem. J.* **351**:19-31. doi:
695 10.1042/0264-6021:3510019, PMID: 11001876
696 Du, Z., H. Su, W. Wang, L. Ye, H. Wei, Z. Peng, I. Anishchenko, D. Baker, and J. Yang.
697 2021. The trRosetta server for fast and accurate protein structure prediction. *Nat.*
698 *Protoc.* **16**:5634-5651. doi: 10.1038/s41596-021-00628-9, PMID: 34759384
699 Essmann, U., L. Perera, M.L. Berkowitz, T. Darden, H. Lee, and L.G. Pedersen. 1995. A
700 smooth particle mesh Ewald method. *J. Chem. Phys.* **103**:8577-8593. doi:
701 10.1063/1.470117
702 Gao, J., R. Kurre, J. Rose, S. Walter, F. Frohlich, J. Piehler, F. Reggiori, and C.
703 Ungermann. 2020. Function of the SNARE Ykt6 on autophagosomes requires
704 the Dsl1 complex and the Atg1 kinase complex. *EMBO Rep.* **21**:e50733. doi:
705 10.15252/embr.202050733, PMID: 33025734
706 Gozani, O., P. Karuman, D.R. Jones, D. Ivanov, J. Cha, A.A. Lugovskoy, C.L. Baird, H.
707 Zhu, S.J. Field, S.L. Lessnick, J. Villasenor, B. Mehrotra, J. Chen, V.R. Rao, J.S.
708 Brugge, C.G. Ferguson, B. Payrastre, D.G. Myszka, L.C. Cantley, G. Wagner, N.
709 Divecha, G.D. Prestwich, and J. Yuan. 2003. The PHD finger of the chromatin-
710 associated protein ING2 functions as a nuclear phosphoinositide receptor. *Cell.*
711 **114**:99-111. doi: 10.1016/s0092-8674(03)00480-x, PMID: 12859901
712 Guo, B., Q. Liang, L. Li, Z. Hu, F. Wu, P. Zhang, Y. Ma, B. Zhao, A.L. Kovacs, Z.
713 Zhang, D. Feng, S. Chen, and H. Zhang. 2014. O-GlcNAc-modification of
714 SNAP-29 regulates autophagosome maturation. *Nat. Cell Biol.* **16**:1215-1226.

715 doi: 10.1038/ncb3066, PMID: 25419848
716 Hammond, G.R., M.J. Fischer, K.E. Anderson, J. Holdich, A. Koteci, T. Balla, and R.F.
717 Irvine. 2012. PI4P and PI(4,5)P_2 are essential but independent lipid determinants
718 of membrane identity. *Science*. **337**:727-730. doi: 10.1126/science.1222483,
719 PMID: 22722250
720 Hammond, G.R., M.P. Machner, and T. Balla. 2014. A novel probe for
721 phosphatidylinositol 4-phosphate reveals multiple pools beyond the Golgi. *J.*
722 *Cell Biol.* **205**:113-126. doi: 10.1083/jcb.201312072, PMID: 24711504
723 Hanada, K. 2006. Discovery of the molecular machinery CERT for endoplasmic
724 reticulum-to-Golgi trafficking of ceramide. *Mol. Cell. Biochem.* **286**:23-31. doi:
725 10.1007/s11010-005-9044-z, PMID: 16601923
726 Hara, T., A. Takamura, C. Kishi, S. Iemura, T. Natsume, J.L. Guan, and N. Mizushima.
727 2008. FIP200, a ULK-interacting protein, is required for autophagosome
728 formation in mammalian cells. *J. Cell Biol.* **181**:497-510. doi:
729 10.1083/jcb.200712064, PMID: 18443221
730 Heo, W.D., T. Inoue, W.S. Park, M.L. Kim, B.O. Park, T.J. Wandless, and T. Meyer.
731 2006. PI(3,4,5)P3 and PI(4,5)P2 lipids target proteins with polybasic clusters to
732 the plasma membrane. *Science*. **314**:1458-1461. doi: 10.1126/science.1134389,
733 PMID: 17095657
734 Horie, C., H. Suzuki, M. Sakaguchi, and K. Mihara. 2002. Characterization of signal
735 that directs C-tail-anchored proteins to mammalian mitochondrial outer
736 membrane. *Mol. Biol. Cell*. **13**:1615-1625. doi: 10.1091/mbc.01-12-0570,
737 PMID: 12006657
738 Huang, J., S. Rauscher, G. Nawrocki, T. Ran, M. Feig, B.L. de Groot, H. Grubmuller,
739 and A.D. MacKerell, Jr. 2017. CHARMM36m: an improved force field for
740 folded and intrinsically disordered proteins. *Nat. Methods*. **14**:71-73. doi:
741 10.1038/nmeth.4067, PMID: 27819658
742 Itakura, E., C. Kishi-Itakura, and N. Mizushima. 2012. The hairpin-type tail-anchored
743 SNARE syntaxin 17 targets to autophagosomes for fusion with
744 endosomes/lysosomes. *Cell*. **151**:1256-1269. doi: 10.1016/j.cell.2012.11.001,
745 PMID: 23217709
746 Jo, S., T. Kim, V.G. Iyer, and W. Im. 2008. CHARMM-GUI: a web-based graphical user
747 interface for CHARMM. *J. Comput. Chem.* **29**:1859-1865. doi:
748 10.1002/jcc.20945, PMID: 18351591
749 Judith, D., H.B.J. Jefferies, S. Boeing, D. Frith, A.P. Snijders, and S.A. Tooze. 2019.
750 ATG9A shapes the forming autophagosome through Arfaptin 2 and

751 phosphatidylinositol 4-kinase IIIβ. *J. Cell Biol.* **218**:1634-1652. doi:
752 10.1083/jcb.201901115, PMID: 30917996
753 Jung, J., T. Mori, C. Kobayashi, Y. Matsunaga, T. Yoda, M. Feig, and Y. Sugita. 2015.
754 GENESIS: a hybrid-parallel and multi-scale molecular dynamics simulator with
755 enhanced sampling algorithms for biomolecular and cellular simulations. *Wiley*
756 *Interdiscip. Rev. Comput. Mol. Sci.* **5**:310-323. doi: 10.1002/wcms.1220, PMID:
757 26753008
758 Kabeya, Y., N. Mizushima, T. Ueno, A. Yamamoto, T. Kirisako, T. Noda, E. Kominami,
759 Y. Ohsumi, and T. Yoshimori. 2000. LC3, a mammalian homologue of yeast
760 Apg8p, is localized in autophagosome membranes after processing. *EMBO J.*
761 **19**:5720-5728. doi: 10.1093/emboj/19.21.5720, PMID: 11060023
762 Kassas, N., E. Tanguy, T. Thahouly, L. Fouillen, D. Heintz, S. Chasserot-Golaz, M.F.
763 Bader, N.J. Grant, and N. Vitale. 2017. Comparative characterization of
764 phosphatidic acid sensors and their localization during frustrated phagocytosis.
765 *J. Biol. Chem.* **292**:4266-4279. doi: 10.1074/jbc.M116.742346, PMID:
766 28115519
767 Kitamura, T., Y. Koshino, F. Shibata, T. Oki, H. Nakajima, T. Nosaka, and H. Kumagai.
768 2003. Retrovirus-mediated gene transfer and expression cloning: powerful tools
769 in functional genomics. *Exp. Hematol.* **31**:1007-1014. doi: S0301472X03002601
770 [pii], PMID: 14585362
771 Koyama-Honda, I., E. Itakura, T.K. Fujiwara, and N. Mizushima. 2013. Temporal
772 analysis of recruitment of mammalian ATG proteins to the autophagosome
773 formation site. *Autophagy*. **9**:1491-1499. doi: 10.4161/auto.25529, PMID:
774 23884233
775 Kumar, S., A. Jain, F. Farzam, J. Jia, Y. Gu, S.W. Choi, M.H. Mudd, A. Claude-Taupin,
776 M.J. Wester, K.A. Lidke, T.E. Rusten, and V. Deretic. 2018a. Mechanism of
777 Stx17 recruitment to autophagosomes via IRGM and mammalian Atg8 proteins.
778 *J. Cell Biol.* **217**:997-1013. doi: 10.1083/jcb.201708039, PMID: 29420192
779 Kumar, S., G. Stecher, M. Li, C. Knyaz, and K. Tamura. 2018b. MEGA X: Molecular
780 evolutionary genetics analysis across computing platforms. *Mol. Biol. Evol.*
781 **35**:1547-1549. doi: 10.1093/molbev/msy096, PMID: 29722887
782 Kurokawa, Y., A. Yoshida, E. Fujii, K. Tomioku, H. Hayashi, K. Tanabe, and A. Fujita.
783 2019. Phosphatidylinositol 4-phosphate on Rab7-positive autophagosomes
784 revealed by the freeze-fracture replica labeling. *Traffic*. **20**:82-95. doi:
785 10.1111/tra.12623, PMID: 30426618
786 Laczkó-Dobos, H., A. Bhattacharjee, A.K. Maddali, A. Kincses, H. Abuammar, K.

Sebők-Nagy, T. Páli, A. Dér, T. Hegedűs, G. Csordás, and G. Juhász. 2024. PtdIns4P is required for the autophagosomal recruitment of STX17 (syntaxin 17) to promote lysosomal fusion. *Autophagy*. **in press**.

Lemmon, M.A. 2008. Membrane recognition by phospholipid-binding domains. *Nat. Rev. Mol. Cell Biol.* **9**:99-111. doi: 10.1038/nrm2328, PMID: 18216767

Levine, T.P., and S. Munro. 1998. The pleckstrin homology domain of oxysterol-binding protein recognises a determinant specific to Golgi membranes. *Curr. Biol.* **8**:729-739. doi: 10.1016/s0960-9822(98)70296-9, PMID: 9651677

Li, J., Z. Gao, D. Zhao, L. Zhang, X. Qiao, Y. Zhao, H. Ding, P. Zhang, J. Lu, J. Liu, H. Jiang, C. Luo, and C. Chen. 2017. PI-273, a Substrate-Competitive, Specific Small-Molecule Inhibitor of PI4KIIalpha, Inhibits the Growth of Breast Cancer Cells. *Cancer Res.* **77**:6253-6266. doi: 10.1158/0008-5472.CAN-17-0484, PMID: 28827373

Li, L., X. Shi, X. Guo, H. Li, and C. Xu. 2014. Ionic protein-lipid interaction at the plasma membrane: what can the charge do? *Trends Biochem. Sci.* **39**:130-140. doi: 10.1016/j.tibs.2014.01.002, PMID: 24534649

Liu, H., W. Shao, W. Liu, W. Shang, J.P. Liu, L. Wang, and C. Tong. 2023. PtdIns4P exchange at endoplasmic reticulum-autolysosome contacts is essential for autophagy and neuronal homeostasis. *Autophagy*:online ahead of print. doi: 10.1080/15548627.2023.2222556, PMID: 37289040

Lu, J., W. Dong, Y. Tao, and Y. Hong. 2021. Electrostatic plasma membrane targeting contributes to Dlg function in cell polarity and tumorigenesis. *Development*. **148**:dev196956. doi: 10.1242/dev.196956, PMID: 33688074

Manford, A., T. Xia, A.K. Saxena, C. Stefan, F. Hu, S.D. Emr, and Y. Mao. 2010. Crystal structure of the yeast Sac1: implications for its phosphoinositide phosphatase function. *EMBO J.* **29**:1489-1498. doi: 10.1038/emboj.2010.57, PMID: 20389282

Matsui, T., P. Jiang, S. Nakano, Y. Sakamaki, H. Yamamoto, and N. Mizushima. 2018. Autophagosomal YKT6 is required for fusion with lysosomes independently of syntaxin 17. *J. Cell Biol.* **217**:2633-2645. doi: 10.1083/jcb.201712058, PMID: 29789439

Mizushima, N., and B. Levine. 2020. Autophagy in human diseases. *N. Engl. J. Med.* **383**:1564-1576. doi: 10.1056/NEJMra2022774, PMID: 33053285

Moravcevic, K., C.L. Oxley, and M.A. Lemmon. 2012. Conditional peripheral membrane proteins: facing up to limited specificity. *Structure*. **20**:15-27. doi: 10.1016/j.str.2011.11.012, PMID: 22193136

Morita, K., Y. Hama, T. Izume, N. Tamura, T. Ueno, Y. Yamashita, Y. Sakamaki, K. Mimura, H. Morishita, W. Shihoya, O. Nureki, H. Mano, and N. Mizushima. 2018. Genome-wide CRISPR screen identifies TMEM41B as a gene required for autophagosome formation. *J. Cell Biol.* **217**:3817-3828. doi: 10.1083/jcb.201804132, PMID: 30093494

Nguyen, T.N., B.S. Padman, J. Usher, V. Oorschot, G. Ramm, and M. Lazarou. 2016. Atg8 family LC3/GABARAP proteins are crucial for autophagosome-lysosome fusion but not autophagosome formation during PINK1/Parkin mitophagy and starvation. *J. Cell Biol.* **215**:857-874. doi: 10.1083/jcb.201607039, PMID: 27864321

Ohkubo, Y.Z., T.V. Pogorelov, M.J. Arcario, G.A. Christensen, and E. Tajkhorshid. 2012. Accelerating membrane insertion of peripheral proteins with a novel membrane mimetic model. *Biophys. J.* **102**:2130-2139. doi: 10.1016/j.bpj.2012.03.015, PMID: 22824277

Platre, M.P., and Y. Jaillais. 2016. Guidelines for the Use of Protein Domains in Acidic Phospholipid Imaging. *Methods Mol. Biol*. **1376**:175-194. doi: 10.1007/978-1-4939-3170-5_15, PMID: 26552684

Platre, M.P., L.C. Noack, M. Doumane, V. Bayle, M.L.A. Simon, L. Maneta-Peyret, L. Fouillen, T. Stanislas, L. Armengot, P. Pejchar, M.C. Caillaud, M. Potocky, A. Copic, P. Moreau, and Y. Jaillais. 2018. A combinatorial lipid code shapes the electrostatic landscape of plant endomembranes. *Dev. Cell*. **45**:465-480 e411. doi: 10.1016/j.devcel.2018.04.011, PMID: 29754803

Quigley, D., and M.I. Probert. 2004. Langevin dynamics in constant pressure extended systems. *J. Chem. Phys.* **120**:11432-11441. doi: 10.1063/1.1755657, PMID: 15268177

Rao, M., V. Okreglak, U.S. Chio, H. Cho, P. Walter, and S.O. Shan. 2016. Multiple selection filters ensure accurate tail-anchored membrane protein targeting. *eLife*. **5**:e21301. doi: 10.7554/eLife.21301, PMID: 27925580

Reuter, L., T. Schmidt, P. Manishankar, C. Throm, J. Keicher, A. Bock, I. Droste-Borel, and C. Oecking. 2021. Light-triggered and phosphorylation-dependent 14-3-3 association with NON-PHOTOTROPIC HYPOCOTYL 3 is required for hypocotyl phototropism. *Nat. Commun.* **12**:6128. doi: 10.1038/s41467-021-26332-6, PMID: 34675219

Ryckaert, J.-P., G. Ciccotti, and H.J.C. Berendsen. 1977. Numerical integration of the cartesian equations of motion of a system with constraints: molecular dynamics of n-alkanes. *J. Comput. Phys.* **23**:327-341. doi: 10.1016/0021-9991(77)90098-5

859 Saitoh, T., H. Nakano, N. Yamamoto, and S. Yamaoka. 2002. Lymphotoxin-β receptor
860 mediates NEMO-independent NF-κB activation. *FEBS Lett.* **532**:45-51. doi:
861 10.1016/s0014-5793(02)03622-0, PMID: 12459460
862 Sanchez-Martin, P., F. Kriegenburg, L. Alves, J. Adam, J. Elsaesser, R. Babic, H.
863 Mancilla, M. Licheva, G. Tascher, C. Munch, S. Eimer, and C. Kraft. 2023.
864 ULK1-mediated phosphorylation regulates the conserved role of YKT6 in
865 autophagy. *J. Cell Sci.* **136**:jcs260546. doi: 10.1242/jcs.260546, PMID:
866 36644903
867 Schink, K.O., K.W. Tan, and H. Stenmark. 2016. Phosphoinositides in Control of
868 Membrane Dynamics. *Annu. Rev. Cell Dev. Biol.* **32**:143-171. doi:
869 10.1146/annurev-cellbio-111315-125349, PMID: 27576122
870 Schmitt, D., S. Bozkurt, P. Henning-Domres, H. Huesmann, S. Eimer, L. Bindila, C.
871 Behrends, E. Boyle, F. Wilfling, G. Tascher, C. Munch, C. Behl, and A. Kern.
872 2022. Lipid and protein content profiling of isolated native autophagic vesicles.
873 *EMBO Rep.* **23**:e53065. doi: 10.15252/embr.202153065, PMID: 36215690
874 Sengupta, N., M. Jovic, E. Barnaeva, D.W. Kim, X. Hu, N. Southall, M. Dejmek, I.
875 Mejdrova, R. Nencka, A. Baumlova, D. Chalupska, E. Boura, M. Ferrer, J.
876 Marugan, and T. Balla. 2019. A large scale high-throughput screen identifies
877 chemical inhibitors of phosphatidylinositol 4-kinase type II alpha. *J. Lipid Res.*
878 **60**:683-693. doi: 10.1194/jlr.D090159, PMID: 30626625
879 Sharma, A., M. Mariappan, S. Appathurai, and R.S. Hegde. 2010. In vitro dissection of
880 protein translocation into the mammalian endoplasmic reticulum. *Methods Mol.*
881 *Biol*. **619**:339-363. doi: 10.1007/978-1-60327-412-8_20, PMID: 20419420
882 Simon, M.L., M.P. Platre, M.M. Marques-Bueno, L. Armengot, T. Stanislas, V. Bayle,
883 M.C. Caillaud, and Y. Jaillais. 2016. A PtdIns(4)P-driven electrostatic field
884 controls cell membrane identity and signalling in plants. *Nat. Plants*. **2**:16089.
885 doi: 10.1038/nplants.2016.89, PMID: 27322096
886 Soreng, K., T.P. Neufeld, and A. Simonsen. 2018. Membrane trafficking in autophagy.
887 *Int. Rev. Cell. Mol. Biol*. **336**:1-92. doi: 10.1016/bs.ircmb.2017.07.001, PMID:
888 29413888
889 Sugiki, T., K. Takeuchi, T. Yamaji, T. Takano, Y. Tokunaga, K. Kumagai, K. Hanada, H.
890 Takahashi, and I. Shimada. 2012. Structural basis for the Golgi association by
891 the pleckstrin homology domain of the ceramide trafficking protein (CERT). *J.*
892 *Biol. Chem.* **287**:33706-33718. doi: 10.1074/jbc.M112.367730, PMID:
893 22869376
894 Synek, L., R. Pleskot, J. Sekeres, N. Serrano, N. Vukasinovic, J. Ortmannova, M.

895 Klejchova, P. Pejchar, K. Batystova, M. Gutkowska, E. Jankova-Drdova, V.
896 Markovic, T. Pecenkova, J. Santrucek, V. Zarsky, and M. Potocky. 2021. Plasma
897 membrane phospholipid signature recruits the plant exocyst complex via the
898 EXO70A1 subunit. *Proc. Natl. Acad. Sci. U. S. A.* **118**:e2105287118. doi:
899 10.1073/pnas.2105287118, PMID: 34470819
900 Taguchi-Atarashi, N., M. Hamasaki, K. Matsunaga, H. Omori, N.T. Ktistakis, T.
901 Yoshimori, and T. Noda. 2010. Modulation of local PtdIns3P levels by the PI
902 phosphatase MTMR3 regulates constitutive autophagy. *Traffic*. **11**:468-478. doi:
903 10.1111/j.1600-0854.2010.01034.x, PMID: 20059746
904 Takáts, S., P. Nagy, A. Varga, K. Pircs, M. Kárpáti, K. Varga, A.L. Kovács, K. Hegedűs,
905 and G. Juhász. 2013. Autophagosomal Syntaxin17-dependent lysosomal
906 degradation maintains neuronal function in *Drosophila*. *J. Cell Biol.* **201**:531-
907 539. doi: 10.1083/jcb.201211160, PMID: 23671310
908 Tsuboyama, K., I. Koyama-Honda, Y. Sakamaki, M. Koike, H. Morishita, and N.
909 Mizushima. 2016. The ATG conjugation systems are important for degradation
910 of the inner autophagosomal membrane. *Science*. **354**:1036-1041. doi:
911 10.1126/science.aaf6136, PMID: 27885029
912 van der Schaar, H.M., P. Leyssen, H.J. Thibaut, A. de Palma, L. van der Linden, K.H.
913 Lanke, C. Lacroix, E. Verbeken, K. Conrath, A.M. Macleod, D.R. Mitchell, N.J.
914 Palmer, H. van de Poel, M. Andrews, J. Neyts, and F.J. van Kuppeveld. 2013. A
915 novel, broad-spectrum inhibitor of enterovirus replication that targets host cell
916 factor phosphatidylinositol 4-kinase IIIbeta. *Antimicrob. Agents Chemother.*
917 **57**:4971-4981. doi: 10.1128/AAC.01175-13, PMID: 23896472
918 Varnai, P., and T. Balla. 1998. Visualization of phosphoinositides that bind pleckstrin
919 homology domains: calcium- and agonist-induced dynamic changes and
920 relationship to myo-[3H]inositol-labeled phosphoinositide pools. *J. Cell Biol.*
921 **143**:501-510. doi: 10.1083/jcb.143.2.501, PMID: 9786958
922 Wang, H., H.Q. Sun, X. Zhu, L. Zhang, J. Albanesi, B. Levine, and H. Yin. 2015.
923 GABARAPs regulate PI4P-dependent autophagosome:lysosome fusion. *Proc.*
924 *Natl. Acad. Sci. U. S. A.* **112**:7015-7020. doi: 10.1073/pnas.1507263112, PMID:
925 26038556
926 Wang, Y., H. Que, C. Li, Z. Wu, F. Jian, Y. Zhao, H. Tang, Y. Chen, S. Gao, C.C.L.
927 Wong, Y. Li, C. Zhao, and Y. Rong. 2023. ULK phosphorylation of STX17
928 controls autophagosome maturation via FLNA. *J. Cell Biol.* **222**:e202211025.
929 doi: 10.1083/jcb.202211025, PMID: 37389864
930 Yagita, Y., T. Hiromasa, and Y. Fujiki. 2013. Tail-anchored PEX26 targets peroxisomes

931 via a PEX19-dependent and TRC40-independent class I pathway. *J. Cell Biol.*
932 **200**:651-666. doi: 10.1083/jcb.201211077, PMID: 23460677
933 Yesbolatova, A., Y. Saito, N. Kitamoto, H. Makino-Itou, R. Ajima, R. Nakano, H.
934 Nakaoka, K. Fukui, K. Gamo, Y. Tominari, H. Takeuchi, Y. Saga, K.I. Hayashi,
935 and M.T. Kanemaki. 2020. The auxin-inducible degron 2 technology provides
936 sharp degradation control in yeast, mammalian cells, and mice. *Nat. Commun.*
937 **11**:5701. doi: 10.1038/s41467-020-19532-z, PMID: 33177522
938 Yeung, T., G.E. Gilbert, J. Shi, J. Silvius, A. Kapus, and S. Grinstein. 2008. Membrane
939 phosphatidylserine regulates surface charge and protein localization. *Science*.
940 **319**:210-213. doi: 10.1126/science.1152066, PMID: 18187657
941 Yeung, T., and S. Grinstein. 2007. Lipid signaling and the modulation of surface charge
942 during phagocytosis. *Immunol. Rev.* **219**:17-36. doi: 10.1111/j.1600-
943 065X.2007.00546.x, PMID: 17850479
944 Yeung, T., M. Terebiznik, L. Yu, J. Silvius, W.M. Abidi, M. Philips, T. Levine, A.
945 Kapus, and S. Grinstein. 2006. Receptor activation alters inner surface potential
946 during phagocytosis. *Science*. **313**:347-351. doi: 10.1126/science.1129551,
947 PMID: 16857939
948

949 **Figure legends**

950

951 **Figure 1.** The recruitment of STX17 to autophagosomes is dependent on its positively
952 charged C-terminal region.
953 **(A)** Schematic representation of the structures of STX17 and its C-terminal variants.
954 The positively (orange) and negatively (blue) charged residues are shown. Alanine
955 substitutions are shown in green. TMH, transmembrane helix; CTR, C-terminal region.
956 **(B)** Schematic representation of the localization of ATG5, LC3B, and STX17 during
957 autophagosome formation and maturation. **(C–E)** Mouse embryonic fibroblasts (MEFs)
958 stably expressing mRuby3-LC3B and GFP–STX17TM (containing the two
959 transmembrane helices and the C-terminal region) or its mutants were cultured in
960 starvation medium for 1 h. Quantification of GFP–STX17TM intensity of mRuby3–
961 LC3B-positive ring-like structures ($n > 30$) are shown in the graphs. In box plots, solid
962 horizontal lines indicate medians, boxes indicate the interquartile ranges (25th to 75th
963 percentiles), whiskers indicate the 5th to 95th percentiles, and dots represent outliers.
964 Differences were statistically analyzed by Welch's *t*-test (C) or one-way ANOVA
965 followed by Dunnett's multiple comparison test (D and E). Experiments were
966 performed three times independently. Scale bars, 10 μm (main), 1 μm (inset) (C, D, and
967 E).

968

969 **Figure 2.** The membrane of autophagosomes becomes negatively charged during
970 maturation.
971 **(A)** GFP–STX17TM translated *in vitro* was incubated with rhodamine-labeled
972 liposomes containing the indicated concentrations of phospholipids: 70%
973 phosphatidylcholine (PC), 20% phosphatidylethanolamine (PE), and 10% of either PE,
974 phosphatidylserine (PS), phosphatidylinositol 3-phosphate (PI3P), or
975 phosphatidylinositol 4-phosphate (PI4P). GFP intensities of liposomes are quantified
976 and shown as in Figure 1C ($n > 30$). **(B)** GFP–STX17TM translated *in vitro* was
977 incubated with rhodamine-labeled liposomes containing 70% PC, 20% PE and 10%
978 PI4P in the presence of 1 M NaCl or 1.2 M sucrose. GFP intensities of liposomes were
979 quantified and shown as in Figure 1C ($n > 30$). **(C)** Amino acid sequences of GFP-

980 tagged membrane surface charge probes. The positively charged residues are shown in
981 orange. The farnesylation motif is indicated in green. **(D and E)** Mouse embryonic
982 fibroblasts (MEFs) stably expressing one of the GFP-tagged charge probes and
983 mRuby3-STX17TM (C) or mRuby3–LC3B (D) were cultured in starvation medium for
984 1 h. GFP intensities of mRuby3–STX17TM-positive (C) or mRuby3–LC3B-positive
985 (D) ring-like structures were quantified ($n > 70$). **(F and G)** Time-lapse analysis of
986 MEFs stably expressing the GFP-tagged 1K8Q (E) or 5K4Q (F) charge probes and
987 mRuby3–STX17TM or mRuby3–LC3B cultured in starvation medium.
988 Autophagosomes are indicated by arrows. **(H)** Summary of electrostatic dynamics of
989 autophagosome formation. In box plots, solid horizontal lines indicate medians, boxes
990 indicate the interquartile ranges (25th to 75th percentiles), whiskers indicate the 5th to
991 95th percentiles, and dots represent outliers. Differences were statistically analyzed by
992 Welch's *t*-test (B) or one-way ANOVA followed by Sidak's multiple comparison test
993 (A, C, and D). Experiments were performed three times independently. Scale bars, 1 μm
994 (A, B, F, and G).
995
996 **Figure 3.** Phosphatidylinositol 4-phosphate (PI4P) is enriched in the autophagosomal
997 membrane during maturation.
998 **(A)** Mouse embryonic fibroblasts (MEFs) stably expressing GFP–CERT(PHD) and
999 mRuby3–STX17TM or mRuby3–ATG5 were cultured in starvation medium for 1 h.
1000 GFP intensities of mRuby3-positive structures ($n > 60$) were quantified. In box plots,
1001 solid horizontal lines indicate medians, boxes indicate the interquartile ranges (25th to
1002 75th percentiles), whiskers indicate the 5th to 95th percentiles, and dots represent
1003 outliers. Differences were statistically analyzed by Welch's *t*-test. **(B–D)** Time-lapse
1004 analysis of MEFs stably expressing GFP–CERT(PHD) and mRuby3–ATG5 (B),
1005 WIPI2B–mRuby3 (C), or mRuby3–STX17TM and HaloTag–LC3B (visualized with
1006 SaraFluor 650T HaloTag ligand) (D) cultured in starvation medium. Autophagosomes
1007 are indicated by arrows. Experiments were performed three times independently. Scale
1008 bars, 10 μm (A [main]), 1 μm (A [inset], B–D).
1009
1010 **Figure 4.** STX17 recruitment to autophagosomes depends on phosphatidylinositol 4-

1011 phosphate (PI4P) *in vitro*.
1012 **(A)** Schematic representation of the *in vitro* autophagosome recruitment assay. Isolated
1013 autophagosomes were mixed with mGFP–STX17TM and either recombinant Sac1-
1014 phosphatase domain (Sac1PD) or its phosphatase-dead mutant (C392S). **(B)** Isolation of
1015 mature autophagosomes prior to their fusion with lysosomes. Homogenates of *STX17*
1016 knockout HeLa cells stably expressing mRuby3–LC3B cultured in starvation medium at
1017 1 h were separated by the OptiPrep membrane flotation method. The autophagosome-
1018 containing fraction (#1: LC3-positive and LAMP1-negative) was collected. The
1019 positions of mRuby3–LC3B (black arrowhead) and endogenous LC3B (white
1020 arrowhead) are indicated. **(C)** Purification of recombinant yeast Sac1 (phosphatase
1021 domain, PD) and its phosphatase-dead (C392S) mutant and mGFP–STX17TM from
1022 High Five cells. **(D)** *In vitro* autophagosome association assay. Isolated autophagosomes
1023 were mixed with recombinant Sac1 (WT or C392S) for 30 min and then with mGFP–
1024 STX17TM for another 30 min. Representative images are shown. STX17-positivity
1025 rates were determined across three independent experiments (two of the three
1026 experiments were performed in a blind manner, and 80 autophagosomes were counted
1027 in each experiment). Solid horizontal lines indicate means. Differences were statistically
1028 analyzed by one-way ANOVA followed by Tukey's test. The scale bar, 2.5 μm.
1029
1030 **Figure 5.** Molecular dynamics simulations of phosphatidylinositol 4-phosphate (PI4P)-
1031 dependent STX17TM insertion into membranes.
1032 **(A, C and E)** An example of a time series of simulated results of STX17TM insertion
1033 into a membrane consisting of 70% phosphatidylcholine (PC), 20%
1034 phosphatidylethanolamine (PE), and 10% PI4P (POPI14) (A), 70% PC and 30% PE (C)
1035 or 70% PC, 20% PE and 10% phosphatidylinositol (PI) (E). STX17TM is shown in
1036 blue. Phosphorus in PC, PE, PI4P and PI are indicated by yellow, cyan, red and orange,
1037 respectively. Short-tailed lipids are represented as green sticks. The time evolution
1038 series of (A), (C) and (E) are shown in Videos 1, 2 and 3. **(B, D and F)** Time evolution
1039 of the z-coordinate of the center of mass (z_{cm}) of the transmembrane helices of
1040 STX17TM in the case of membranes with PI4P (B) or PI (F) and without PI4P or PI
1041 (D). Five independent simulation results are represented by solid lines of different

1042 colors. The gray dashed lines indicate the locations of the lipid heads. Scale bars, 5 nm
1043 (A, C, and E). **(G)** Model of the PI4P-driven electrostatic maturation of the
1044 autophagosome and STX17 recruitment.
1045
1046 **Figure 1—figure supplement 1.** Recruitment of STX17 depends on the abundance of
1047 cationic amino acids in the C-terminal region but not on its specific amino acid
1048 sequence.
1049 **(A)** Multiple sequence alignment of STX17 proteins from *Homo sapiens* (Hs), *Mus*
1050 *musculus*, *Danio rerio*, *Ciona intestinalis*, *Drosophila melanogaster* (Dm), and
1051 *Caenorhabditis elegans* (Ce). Identical residues between more than two species are
1052 indicated with gray boxes. Domains of STX17 are indicated with different colors: green,
1053 the Habc domain; magenta, the SNARE domain; blue, transmembrane helix (TMH);
1054 orange, a linker between the TMDs; and purple, the C-terminal region. **(B)** Mouse
1055 embryonic fibroblasts (MEFs) stably expressing mRuby3–LC3B and either GFP-tagged
1056 HsSTX17TM, DsSTX17TM, or CeSTX17TM were cultured in starvation medium for 1
1057 h. GFP–STX17TM intensities of mRuby3–LC3B-positive ring-like structures were
1058 quantified ($n > 30$). In box plots, solid horizontal lines indicate medians, boxes indicate
1059 the interquartile ranges (25th to 75th percentiles), whiskers indicate the 5th to 95th
1060 percentiles, and dots represent outliers. **(C)** MEFs stably expressing one of the GFP-
1061 tagged alanine replacement mutants (shown in Figure 1A) and mRuby3–LC3B were
1062 cultured in starvation medium for 1 h. Quantification results are shown in Figure 1D.
1063 **(D)** MEFs stably expressing one of the GFP-tagged charge replacement mutants (shown
1064 in Figure 1E) and mRuby3–LC3B were cultured in starvation medium for 1 h.
1065 Quantification results are shown in Figure 1E. Experiments were performed three times
1066 independently. Scale bars, 10 μm (main), 1 μm (inset) (B, C, and D).
1067
1068 **Figure 2—figure supplement 1.** The membrane of autophagosomes becomes
1069 negatively charged during maturation.
1070 **(A)** Mouse embryonic fibroblasts stably expressing one of the GFP-tagged charge
1071 probes and mRuby3–LC3B were cultured in starvation medium for 1 h. **(B)** Time-lapse
1072 analysis of MEFs stably expressing GFP–3K6Q and mRuby3–STX17TM or mRuby3–

1073 LC3B cultured in starvation medium. Autophagosomes are indicated by arrows. **(C)**
1074 Time-lapse analysis of MEFs stably expressing one of the GFP-tagged charge probes
1075 and mRuby3–ATG5 cultured in starvation medium. Autophagosomes are indicated by
1076 arrows. Experiments were performed three times independently. Scale bars, 10 μm (A
1077 [main]), 1 μm (A [inset], B, and C).
1078
1079 **Figure 3—figure supplement 1.** Localization of phospholipids in mature
1080 autophagosomes.
1081 **(A)** Mouse embryonic fibroblasts (MEFs) stably expressing the indicated GFP-tagged
1082 phospholipid probe and mRuby3–STX17TM were cultured in starvation medium for 1
1083 h. The following phospholipid probes were used: phosphatidic acid (PA),
1084 Spo20(PABD); PS, Evectin-2; diacylglycerol (DAG), PKD C1ab; PI3P, 2×FYVE; PI4P,
1085 CERT(PHD); PI5P, ING2(PlantHD); PI(3,4)P_2, TAPP1(PHD); PI(4,5)P_2, PLCd1(PHD);
1086 PI(3,5)P_2, TRPML1(PHD); and PIP_3, Btk(PHD). **(B)** MEFs stably expressing GFP–
1087 CERT(PHD) or TRPML1(PHD) were cultured in starvation medium containing
1088 LysoTracker Deep Red for 1 h. **(C)** MEFs stably expressing GFP–PI4KB or GFP–
1089 PI4K2A and mRuby3–LC3B were cultured in starvation medium for 1 h. Experiments
1090 were performed three times independently. Scale bars, 10 μm (main), 1 μm (inset).
1091
1092 **Figure 3—figure supplement 2.** Phosphatidylinositol 4-phosphate (PI4P) is enriched in
1093 mature autophagosomes before fusion with lysosomes.
1094 **(A and B)** Mouse embryonic fibroblasts (MEFs) stably expressing the indicated GFP-
1095 tagged PI4P probe, CERT(PHD)(W33A), FAPP(PHD), OSBP(PHD) or P4M-SidMx2,
1096 and mRuby3–STX17TM or mRuby3–ATG5 were cultured in starvation medium for 1 h.
1097 **(C)** GFP intensities of mRuby3-positive structures ($n > 50$) in (B) were quantified. In
1098 box plots, solid horizontal lines indicate medians, boxes indicate the interquartile ranges
1099 (25th to 75th percentiles), whiskers indicate the 5th to 95th percentiles, and dots
1100 represent outliers. Differences were statistically analyzed by Welch's *t*-test. **(D)** Time-
1101 lapse analysis of MEFs stably expressing GFP–CERT(PHD) cultured in starvation
1102 medium containing LysoTracker Deep Red. **(E)** U2OS cells stably expressing GFP–
1103 CERT(PHD) and mRuby3–LC3B were transfected with siSTX17 and siYKT6. After 3

days, cells were cultured in starvation medium for 1 h, and immunostained with anti-LAMP1 antibodies. **(F)** WT and ATG8 hexa KO HeLa cells stably expressing GFP–STX17TM and transiently expressing mRuby3–CERT(PHD) were cultured in starvation medium for 1 h. Experiments were performed three times independently. Scale bars, 10 μm (A, B, and E [main]), 1 μm (A, B, E [inset], and D).

Figure 4—figure supplement 1. The PI 4-kinase inhibitor NC03 failed to suppress autophagosomal PI4P accumulation and STX17 recruitment.
HEK293T cells stably expressing mRuby3–STX17TM (A) or mRuby3–CERT(PHD) (B) and HaloTag-LC3B were cultured in starvation medium for 1 h and then treated with and without 10 μM NC03 for 10 min. Representative confocal images are shown. STX17TM- or CERT(PHD)-positive rates of LC3B structures per cell (n > 30 cells) are shown in the graphs. Solid horizontal lines indicate medians, boxes indicate the interquartile ranges (25th to 75th percentiles), whiskers indicate the 5th to 95th percentiles, and dots represent outliers. Differences were statistically analyzed by Welch's t-test. Scale bars, 10 μm (main), 1 μm (inset).

Video 1. Molecular dynamics simulations of STX17TM insertion into a phosphatidylinositol 4-phosphate (PI4P)-containing membrane.
STX17TM is shown in blue. Phosphorus in POPC (70%), POPE (20%), and PI4P (10%) are indicated by yellow, cyan, and red spheres, respectively. Short-tailed lipids are represented by green sticks. This video corresponds to Figure 5A.

Video 2. Molecular dynamics simulations of STX17TM insertion into a membrane without phosphatidylinositol 4-phosphate (PI4P).
STX17TM is shown in blue. Phosphorus in POPC (70%) and POPE (30%) are indicated in yellow and cyan, respectively. Short-tailed lipids are represented by green sticks. This video corresponds to Figure 5C.

Video 3. Molecular dynamics simulations of STX17TM insertion into a phosphatidylinositol (PI)-containing membrane.

1135 STX17TM is shown in blue. Phosphorus in POPC (70%), POPE (20%), and PI (10%)
1136 are indicated by yellow, cyan, and orange spheres, respectively. Short-tailed lipids are
1137 represented by green sticks. This video corresponds to Figure 5E.

Figure 1

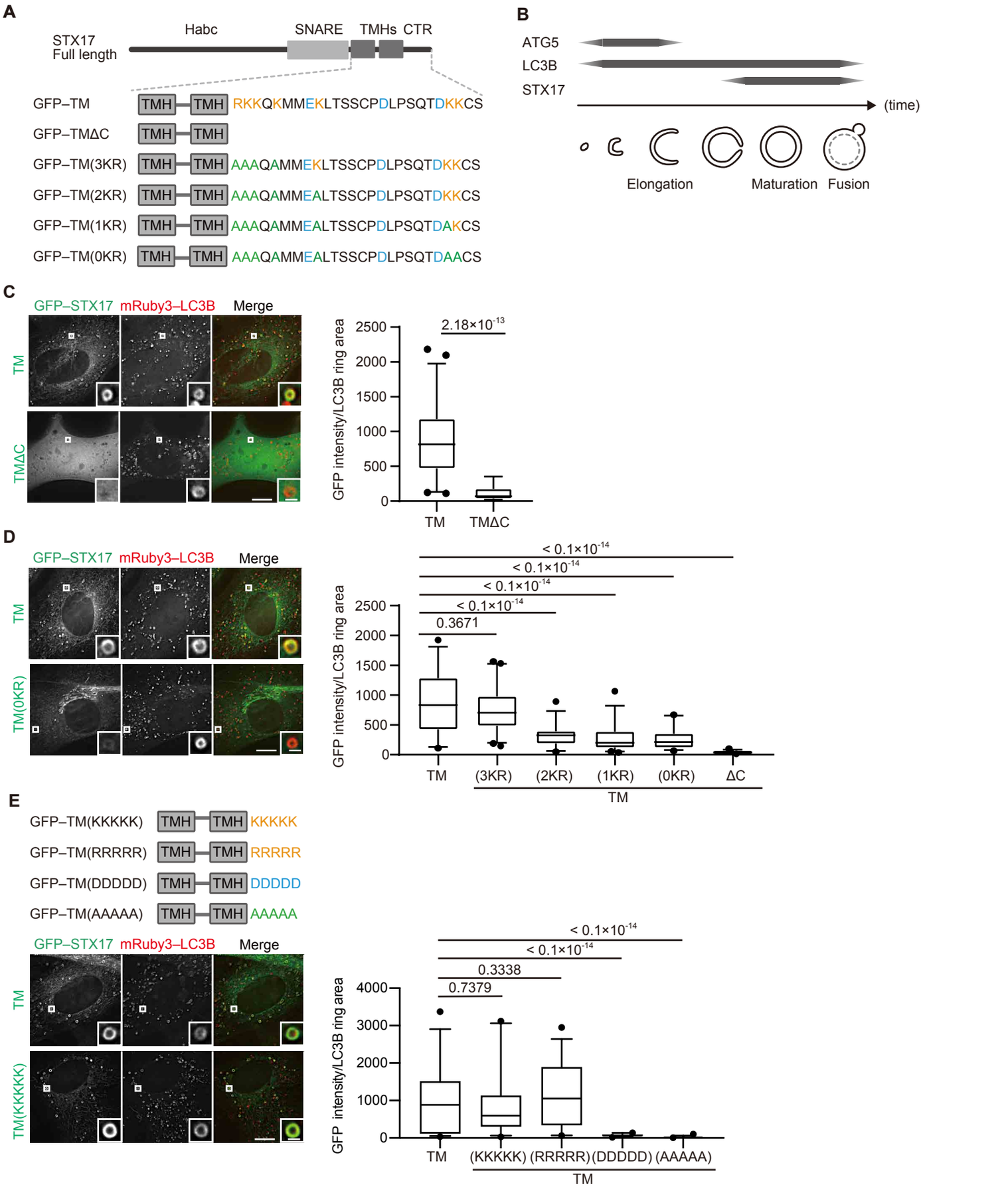

Figure 1. The recruitment of STX17 to autophagosomes is dependent on its positively charged C-terminal region.
(A) Schematic representation of the structures of STX17 and its C-terminal variants. The positively (orange) and negatively (blue) charged residues are shown. Alanine substitutions are shown in green. TMH, transmembrane helix; CTR, C-terminal region. **(B)** Schematic representation of the localization of ATG5, LC3B, and STX17 during autophagosome formation and maturation. **(C–E)** Mouse embryonic fibroblasts (MEFs) stably expressing mRuby3-LC3B and GFP–STX17TM (containing the two transmembrane helices and the C-terminal region) or its mutants were cultured in starvation medium for 1 h. Quantification of GFP–STX17TM intensity of mRuby3–LC3B-positive ring-like structures ($n > 30$) are shown in the graphs. In box plots, solid horizontal lines indicate medians, boxes indicate the interquartile ranges (25th to 75th percentiles), whiskers indicate the 5th to 95th percentiles, and dots represent outliers. Differences were statistically analyzed by Welch' s *t*-test (C) or one-way ANOVA followed by Dunnett' s multiple comparison test (D and E). Experiments were performed three times independently. Scale bars, 10 μm (main), 1 μm (inset) (C, D, and E).

Figure 1−figure supplement 1

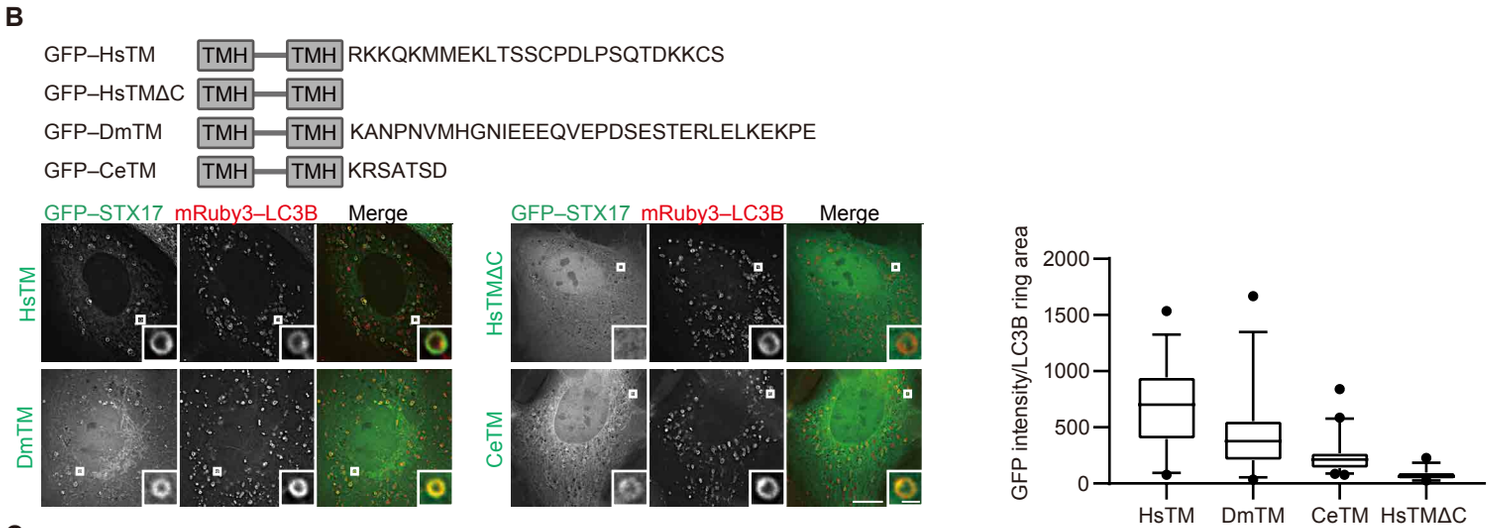

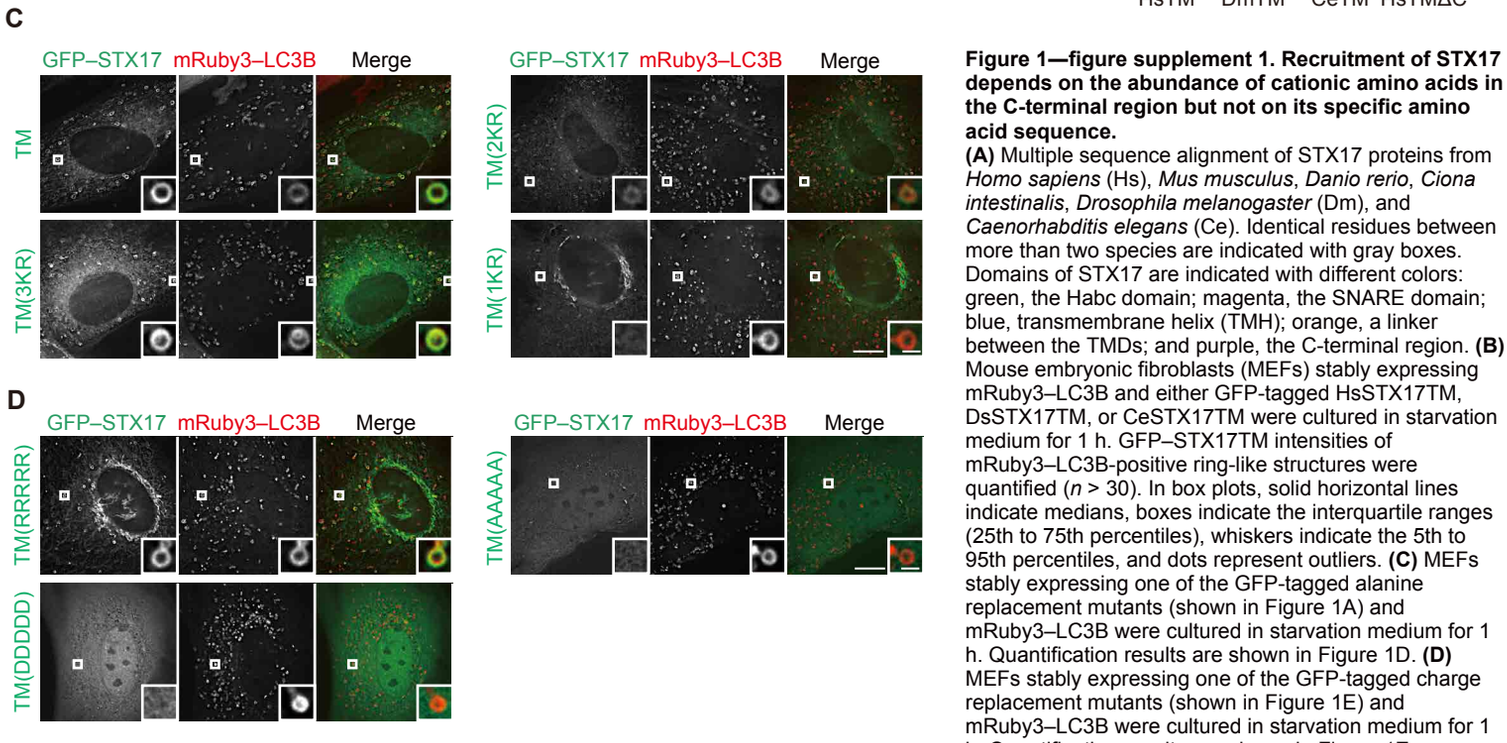

Figure 1—figure supplement 1. Recruitment of STX17 depends on the abundance of cationic amino acids in the C-terminal region but not on its specific amino acid sequence.
(A) Multiple sequence alignment of STX17 proteins from *Homo sapiens* (Hs), *Mus musculus*, *Danio rerio*, *Ciona intestinalis*, *Drosophila melanogaster* (Dm), and *Caenorhabditis elegans* (Ce). Identical residues between more than two species are indicated with gray boxes. Domains of STX17 are indicated with different colors: green, the Habc domain; magenta, the SNARE domain; blue, transmembrane helix (TMH); orange, a linker between the TMDs; and purple, the C-terminal region. **(B)** Mouse embryonic fibroblasts (MEFs) stably expressing mRuby3–LC3B and either GFP-tagged HsSTX17TM, DsSTX17TM, or CeSTX17TM were cultured in starvation medium for 1 h. GFP–STX17TM intensities of mRuby3–LC3B-positive ring-like structures were quantified (n > 30). In box plots, solid horizontal lines indicate medians, boxes indicate the interquartile ranges (25th to 75th percentiles), whiskers indicate the 5th to 95th percentiles, and dots represent outliers. **(C)** MEFs stably expressing one of the GFP-tagged alanine replacement mutants (shown in Figure 1A) and mRuby3–LC3B were cultured in starvation medium for 1 h. Quantification results are shown in Figure 1D. **(D)** MEFs stably expressing one of the GFP-tagged charge replacement mutants (shown in Figure 1E) and mRuby3–LC3B were cultured in starvation medium for 1 h. Quantification results are shown in Figure 1E. Experiments were performed three times independently. Scale bars, 10 μm (main), 1 μm (inset) (B, C and D).

Figure 2

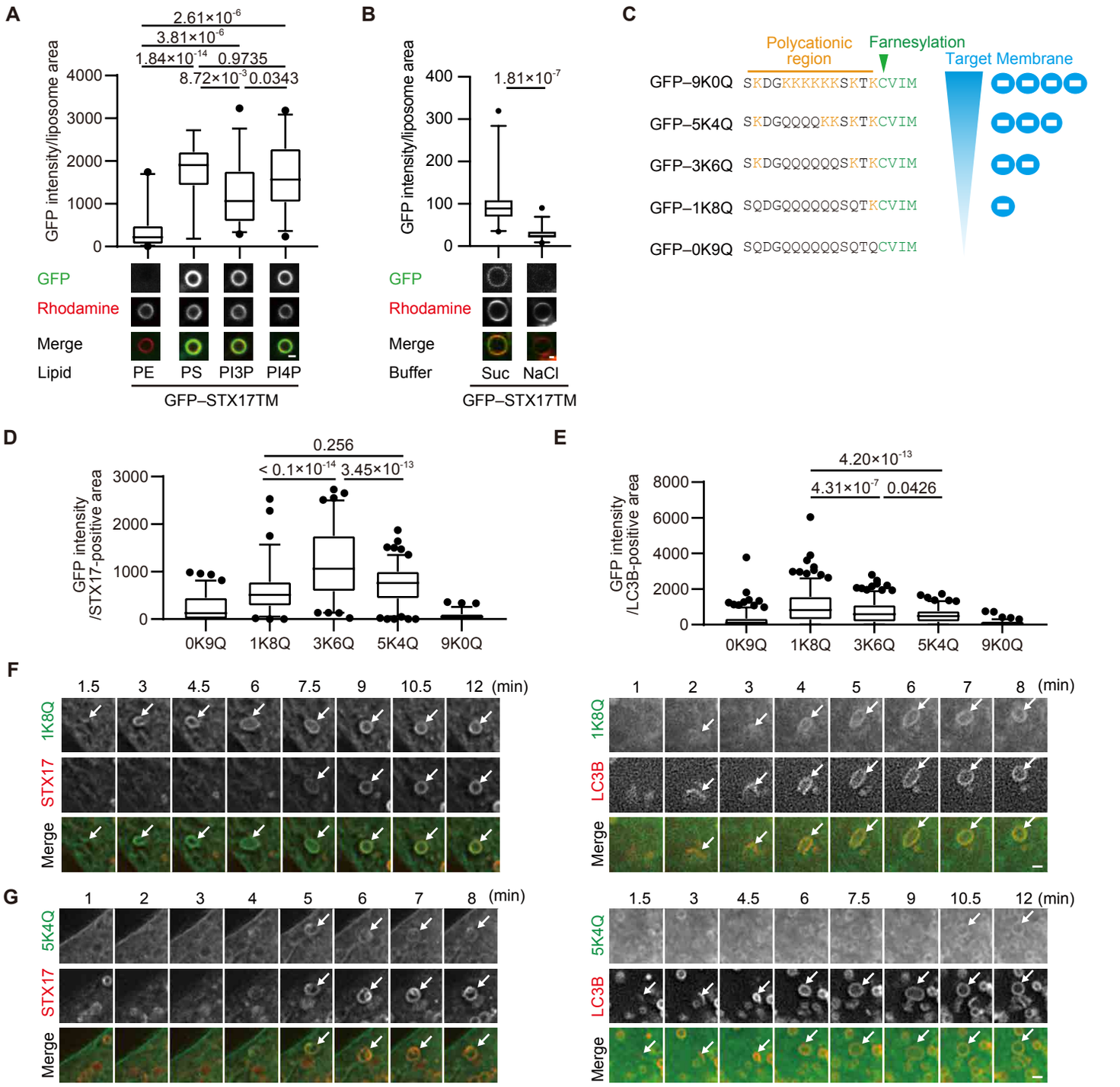

Figure 2. The membrane of autophagosomes becomes negatively charged during maturation.
(A) GFP–STX17TM translated *in vitro* was incubated with rhodamine-labeled liposomes containing the indicated concentrations of phospholipids: 70% phosphatidylcholine (PC), 20% phosphatidylethanolamine (PE), and 10% of either PE, phosphatidylserine (PS), phosphatidylinositol 3-phosphate (PI3P), or phosphatidylinositol 4-phosphate (PI4P). GFP intensities of liposomes are quantified and shown as in Figure 1C ($n > 30$). **(B)** GFP–STX17TM translated *in vitro* was incubated with rhodamine-labeled liposomes containing 70% PC, 20% PE and 10% PI4P in the presence of 1 M NaCl or 1.2 M sucrose. GFP intensities of liposomes were quantified and shown as in Figure 1C ($n > 30$). **(C)** Amino acid sequences of GFP-tagged membrane surface charge probes. The positively charged residues are shown in orange. The farnesylation motif is indicated in green. **(D and E)** Mouse embryonic fibroblasts (MEFs) stably expressing one of the GFP-tagged charge probes and mRuby3-STX17TM (C) or mRuby3–LC3B (D) were cultured in starvation medium for 1 h. GFP intensities of mRuby3–STX17TM-positive (C) or mRuby3–LC3B-positive (D) ring-like structures were quantified ($n > 70$). **(F and G)** Time-lapse analysis of MEFs stably expressing the GFP-tagged 1K8Q (E) or 5K4Q (F) charge probes and mRuby3–STX17TM or mRuby3–LC3B cultured in starvation medium. Autophagosomes are indicated by arrows. **(H)** Summary of electrostatic dynamics of autophagosome formation. In box plots, solid horizontal lines indicate medians, boxes indicate the interquartile ranges (25th to 75th percentiles), whiskers indicate the 5th to 95th percentiles, and dots represent outliers. Differences were statistically analyzed by Welch' s *t*-test (B) or one-way ANOVA followed by Sidak' s multiple comparison test (A, C, and D). Experiments were performed three times independently. Scale bars, 1 μm (A, B, F, and G).

Figure 2−figure supplement 1

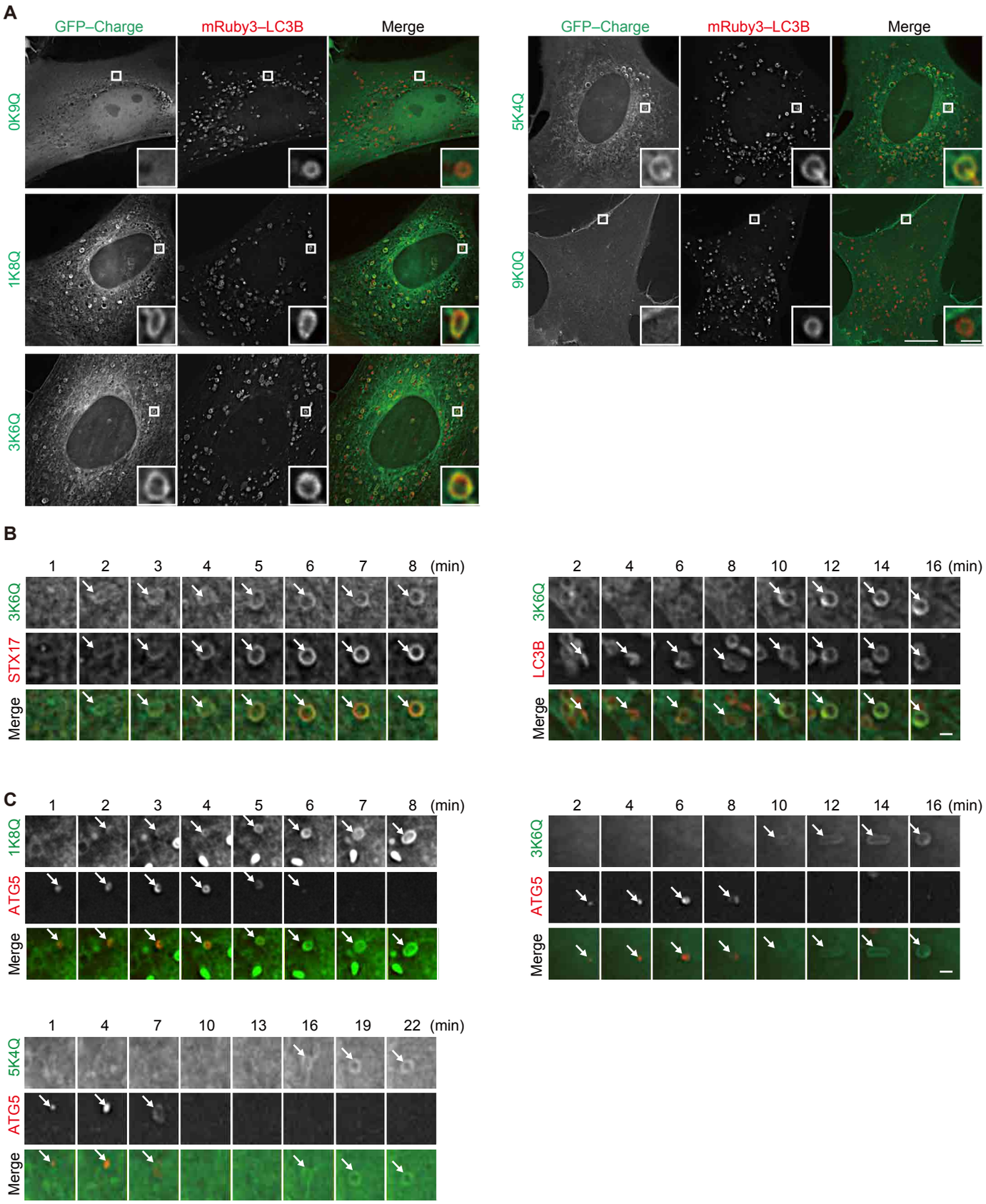

Figure 2—figure supplement 1. The membrane of autophagosomes becomes negatively charged during maturation.
(A) Mouse embryonic fibroblasts stably expressing one of the GFP-tagged charge probes and mRuby3–LC3B were cultured in starvation medium for 1 h. **(B)** Time-lapse analysis of MEFs stably expressing GFP–3K6Q and mRuby3–STX17TM or mRuby3–LC3B cultured in starvation medium. Autophagosomes are indicated by arrows. **(C)** Time-lapse analysis of MEFs stably expressing one of the GFP-tagged charge probes and mRuby3–ATG5 cultured in starvation medium. Autophagosomes are indicated by arrows. Experiments were performed three times independently. Scale bars, 10 μm (A [main]), 1 μm (A [inset], B, and C).

Figure 3

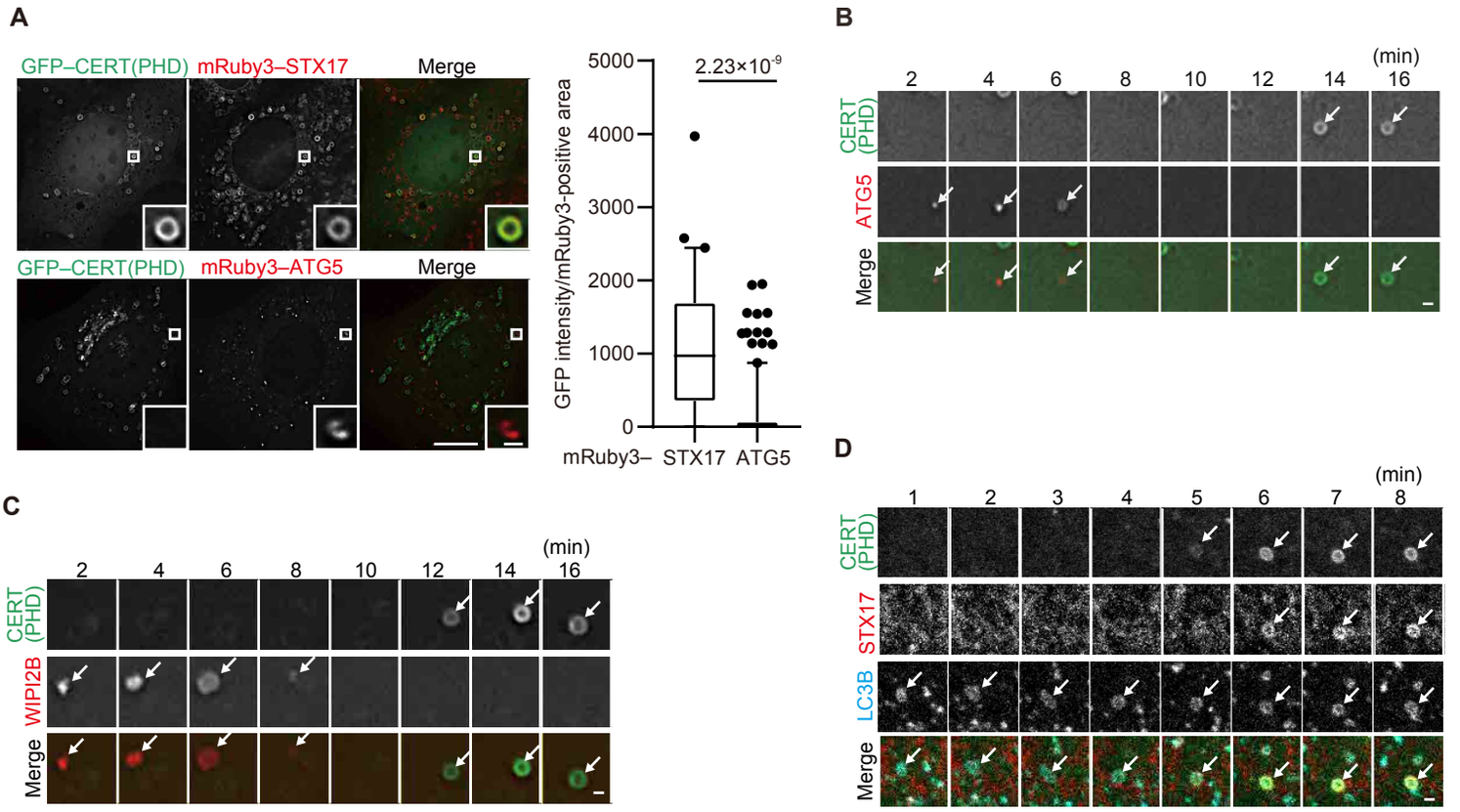

Figure 3. Phosphatidylinositol 4-phosphate (PI4P) is enriched in the autophagosomal membrane during maturation.
(A) Mouse embryonic fibroblasts (MEFs) stably expressing GFP–CERT(PHD) and mRuby3–STX17TM or mRuby3–ATG5 were cultured in starvation medium for 1 h. GFP intensities of mRuby3-positive structures (n > 60) were quantified. In box plots, solid horizontal lines indicate medians, boxes indicate the interquartile ranges (25th to 75th percentiles), whiskers indicate the 5th to 95th percentiles, and dots represent outliers. Differences were statistically analyzed by Welch' s t-test. **(B–D)** Time-lapse analysis of MEFs stably expressing GFP–CERT(PHD) and mRuby3–ATG5 (B), WIPI2B–mRuby3 (C), or mRuby3–STX17TM and HaloTag–LC3B (visualized with SaraFluor 650T HaloTag ligand) (D) cultured in starvation medium. Autophagosomes are indicated by arrows. Experiments were performed three times independently. Scale bars, 10 μm (A [main]), 1 μm (A [inset], B–D).

Figure 3−figure supplement 1

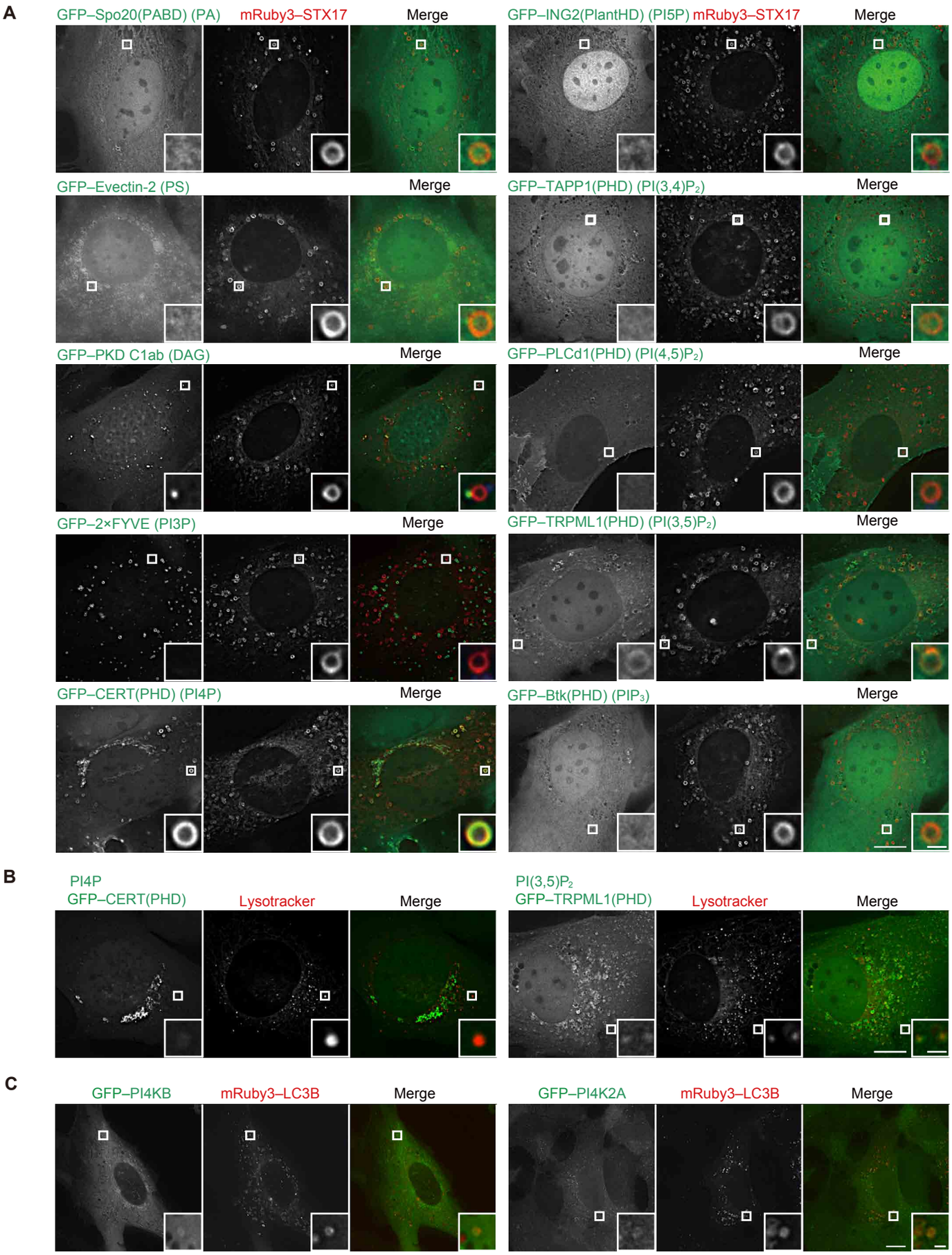

Figure 3—figure supplement 1. Localization of phospholipids in mature autophagosomes.
(A) Mouse embryonic fibroblasts (MEFs) stably expressing the indicated GFP-tagged phospholipid probe and mRuby3–STX17TM were cultured in starvation medium for 1 h. The following phospholipid probes were used: phosphatidic acid (PA), Spo20(PABD); PS, Evectin-2; diacylglycerol (DAG), PKD C1ab; PI3P, 2×FYVE; PI4P, CERT(PHD); PI5P, ING2(PlantHD); PI(3,4)P_2, TAPP1(PHD); PI(4,5)P_2, PLCd1(PHD); PI(3,5)P_2, TRPML1(PHD); and PIP_3, Btk(PHD). **(B)** MEFs stably expressing GFP–CERT(PHD) or TRPML1(PHD) were cultured in starvation medium containing LysoTracker Deep Red for 1 h. **(C)** MEFs stably expressing GFP–PI4KB or GFP–PI4K2A and mRuby3–LC3B were cultured in starvation medium for 1 h. Experiments were performed three times independently. Scale bars, 10 μm (main), 1 μm (inset).

Figure 3−figure supplement 2

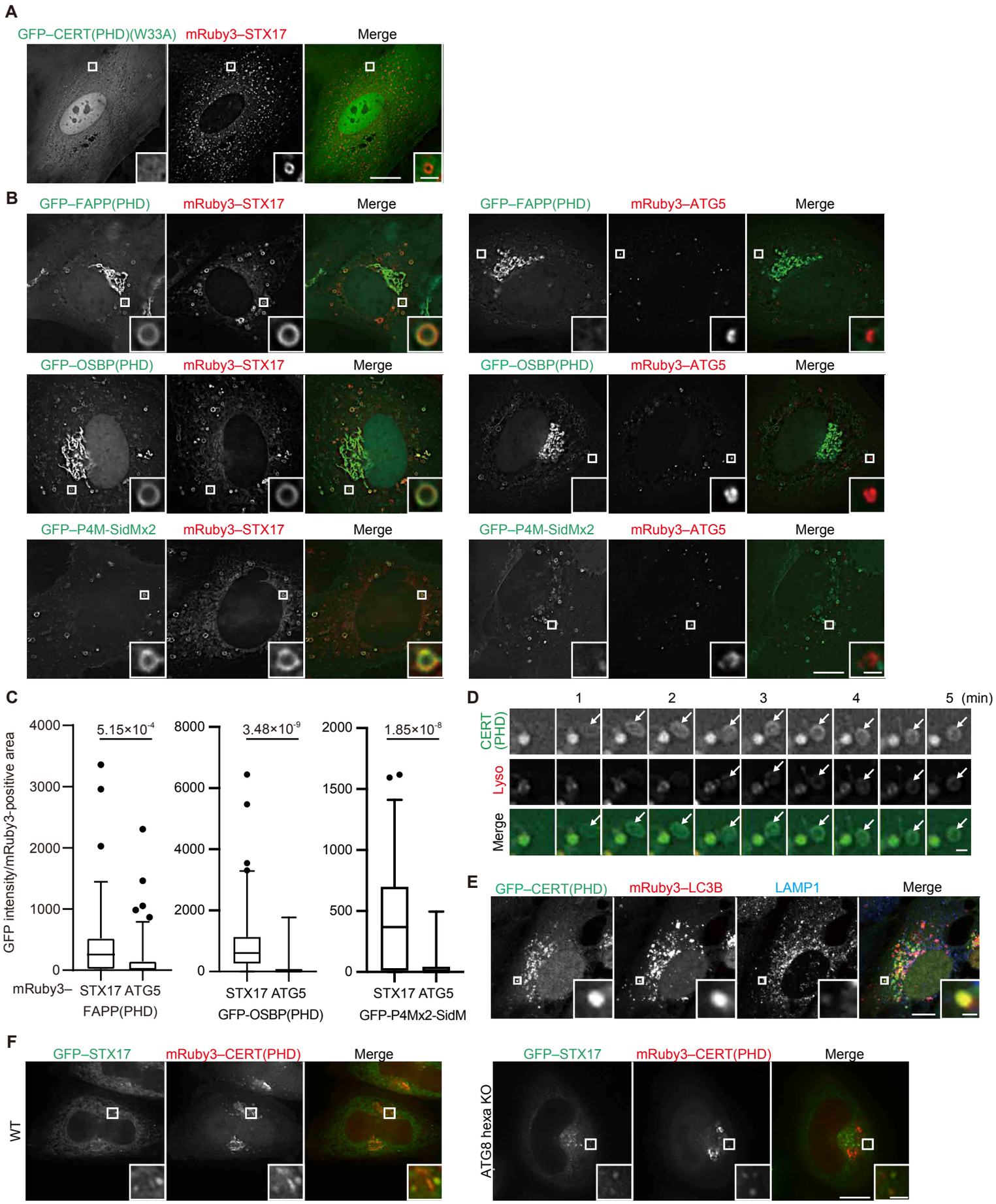

Figure 3—figure supplement 2. Phosphatidylinositol 4-phosphate (PI4P) is enriched in mature autophagosomes before fusion with lysosomes. **(A and B)** Mouse embryonic fibroblasts (MEFs) stably expressing the indicated GFP-tagged indicated PI4P probe, CERT(PHD)(W33A), FAPP(PHD), OSBP(PHD) or P4M-SidMx2, and mRuby3–STX17TM or mRuby3–ATG5 were cultured in starvation medium for 1 h. **(C)** GFP intensities of mRuby3-positive structures ($n > 50$) in (B) were quantified. In box plots, solid horizontal lines indicate medians, boxes indicate the interquartile ranges (25th to 75th percentiles), whiskers indicate the 5th to 95th percentiles, and dots represent outliers. Differences were statistically analyzed by Welch' s *t*-test. **(D)** Time-lapse analysis of MEFs stably expressing GFP–CERT(PHD) cultured in starvation medium containing LysoTracker Deep Red. **(E)** U2OS cells stably expressing GFP–CERT(PHD) and mRuby3–LC3B were transfected with siSTX17 and siYKT6. After 3 days, cells were cultured in starvation medium for 1 h, and immunostained with anti-LAMP1 antibodies. **(F)** WT and ATG8 hexa KO HeLa cells stably expressing GFP–STX17TM and transiently expressing mRuby3–CERT(PHD) were cultured in starvation medium for 1 h. Experiments were performed three times independently. Scale bars, 10 μm (A, B, and E [main]), 1 μm (A, B, E [inset], and D).

Figure 4

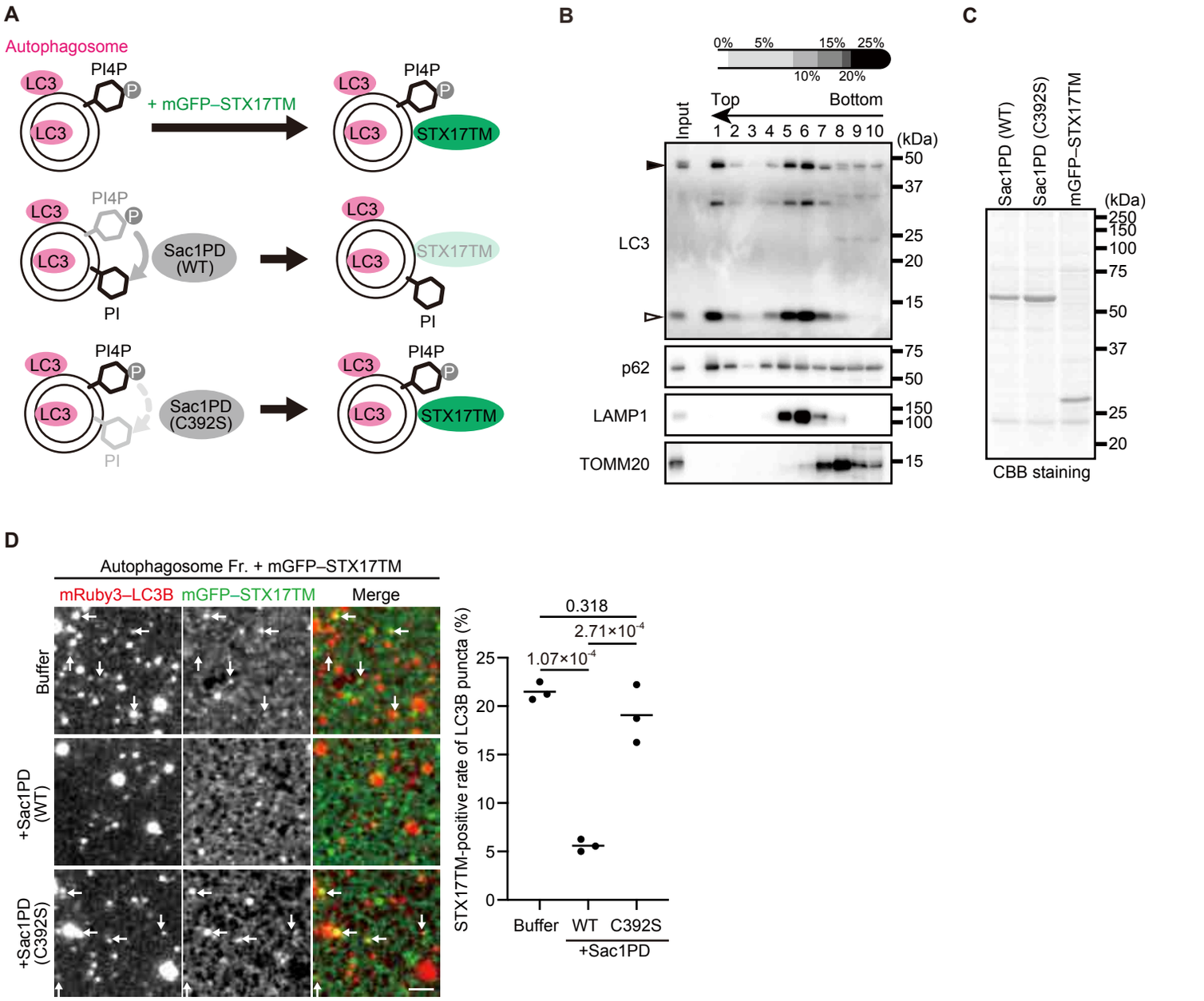

Figure 4. STX17 recruitment to autophagosomes depends on phosphatidylinositol 4-phosphate (PI4P) *in vitro*.
(A) Schematic representation of the *in vitro* autophagosome recruitment assay. Isolated autophagosomes were mixed with mGFP–STX17TM and either recombinant Sac1-phosphatase domain (Sac1PD) or its phosphatase-dead mutant (C392S). **(B)** Isolation of mature autophagosomes prior to their fusion with lysosomes. Homogenates of *STX17* knockout HeLa cells stably expressing mRuby3–LC3B cultured in starvation medium at 1 h were separated by the OptiPrep membrane flotation method. The autophagosome-containing fraction (#1: LC3-positive and LAMP1-negative) was collected. The positions of mRuby3–LC3B (black arrowhead) and endogenous LC3B (white arrowhead) are indicated. **(C)** Purification of recombinant yeast Sac1 (phosphatase domain, PD) and its phosphatase-dead (C392S) mutant and mGFP–STX17TM from High Five cells. **(D)** *In vitro* autophagosome association assay. Isolated autophagosomes were mixed with recombinant Sac1 (WT or C392S) for 30 min and then with mGFP–STX17TM for another 30 min. Representative images are shown. STX17-positivity rates were determined across three independent experiments (two of the three experiments were performed in a blind manner, and 80 autophagosomes were counted in each experiment). Solid horizontal lines indicate means. Differences were statistically analyzed by one-way ANOVA followed by Tukey' s test. The scale bar, 2.5 μm.

Figure 4−figure supplement 1

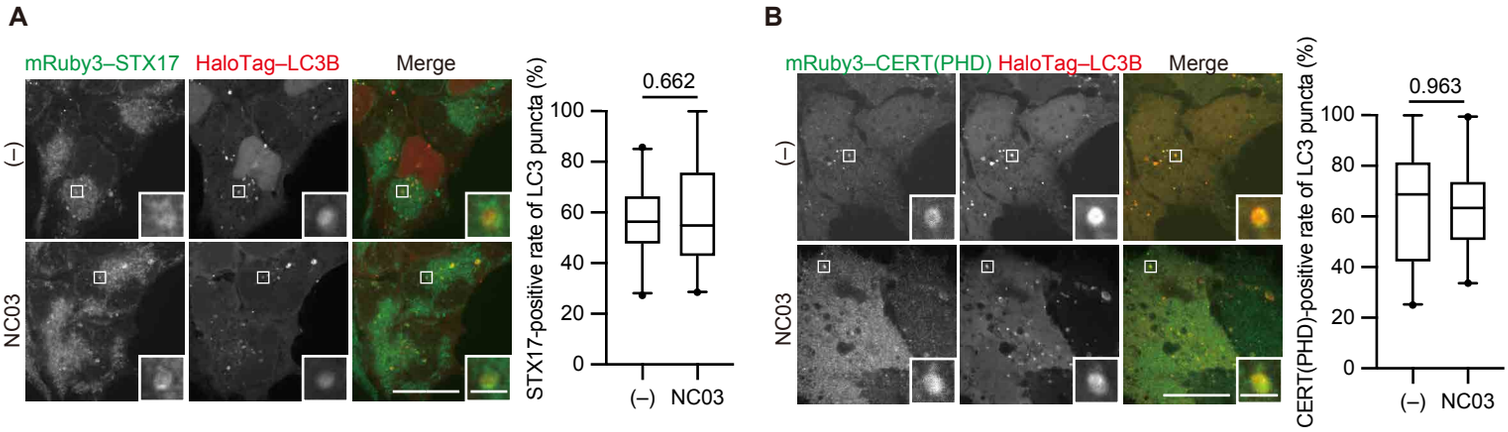

Figure 4—figure supplement 1. The PI 4-kinase inhibitor NC03 failed to suppress autophagosomal PI4P accumulation and STX17 recruitment. HEK293T cells stably expressing mRuby3–STX17TM (A) or mRuby3–CERT(PHD) (B) and HaloTag-LC3B were cultured in starvation medium for 1 h and then treated with and without 10 μM NC03 for 10 min. Representative confocal images are shown. STX17TM- or CERT(PHD)-positive rates of LC3B structures per cell (n > 30 cells) are shown in the graphs. Solid horizontal lines indicate medians, boxes indicate the interquartile ranges (25th to 75th percentiles), whiskers indicate the 5th to 95th percentiles, and dots represent outliers. Differences were statistically analyzed by Welch' s t-test. Scale bars, 10 μm (main), 1 μm (inset).

Figure 5

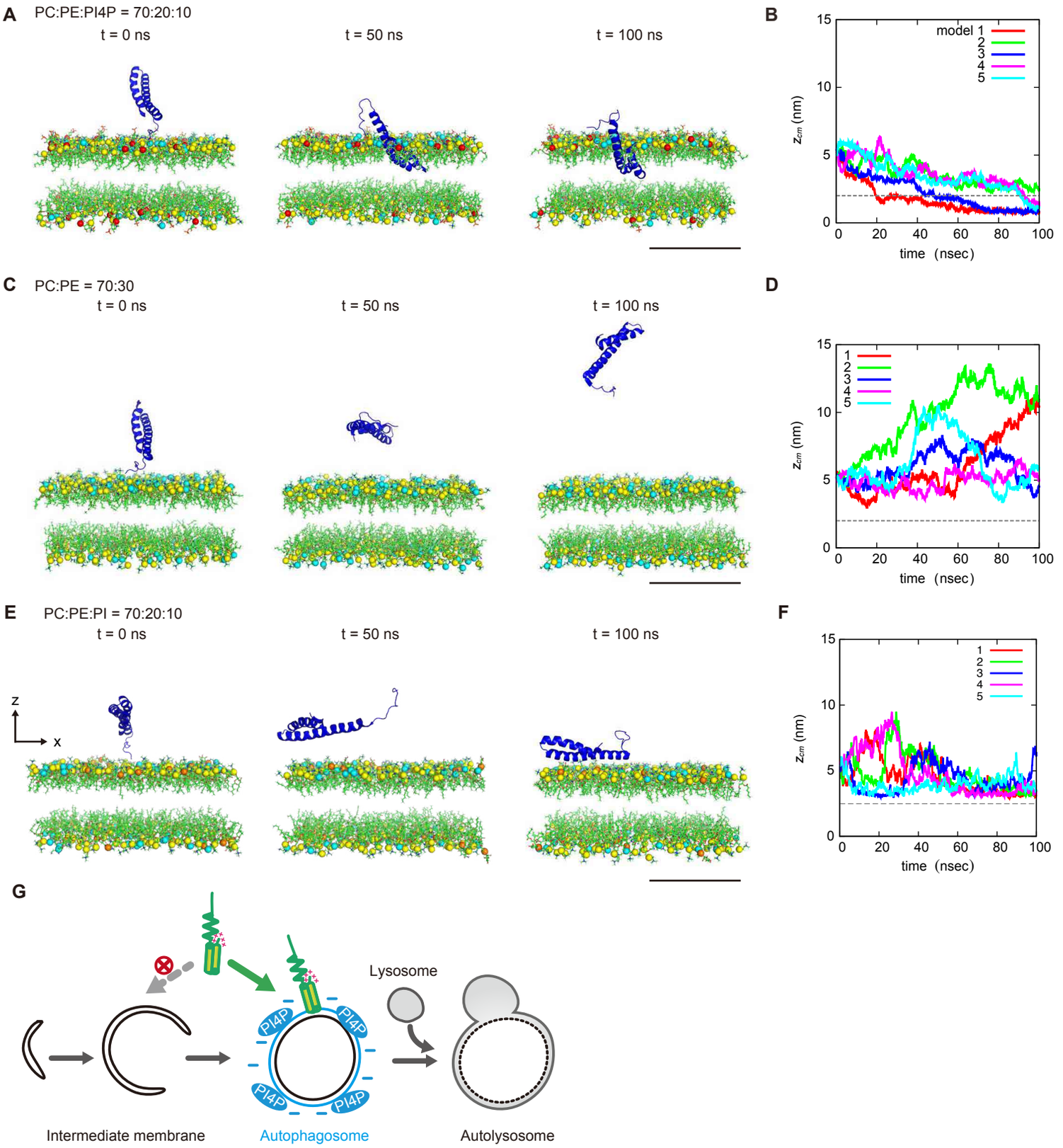

Figure 5. Molecular dynamics simulations of phosphatidylinositol 4-phosphate (PI4P)-dependent STX17TM insertion into membranes.
(A, C and E) An example of a time series of simulated results of STX17TM insertion into a membrane consisting of 70% phosphatidylcholine (PC), 20% phosphatidylethanolamine (PE), and 10% PI4P (POPI14) (A), 70% PC and 30% PE (C) or 70% PC, 20% PE and 10% phosphatidylinositol (PI) (E). STX17TM is shown in blue. Phosphorus in PC, PE, PI4P and PI are indicated by yellow, cyan, red and orange, respectively. Short-tailed lipids are represented as green sticks. The time evolution series of (A), (C) and (E) are shown in Videos 1, 2 and 3. **(B, D and F)** Time evolution of the *z*-coordinate of the center of mass (z_{cm}) of the transmembrane helices of STX17TM in the case of membranes with PI4P (B) or PI (F) and without PI4P or PI (D). Five independent simulation results are represented by solid lines of different colors. The gray dashed lines indicate the locations of the lipid heads. Bars indicate 5 nm (A, C, and E). **(G)** Model of the PI4P-driven electrostatic maturation of the autophagosome and STX17 recruitment.